

**DOE DE-FG26-99FT-40584**

**FINAL REPORT**

**October 2004**

**ADVANCED COMPUTATIONAL MODEL FOR  
THREE-PHASE SLURRY REACTORS**

**Grant Number: DE-FG26-99FT-40584**

**Goodarz Ahmadi**

**Department of Mechanical and Aeronautical Engineering  
Clarkson University**

**Submitted to**

**U.S. Department of Energy**

**National Energy Technology Laboratory**

**TITLE:** ADVANCED COMPUTATIONAL MODEL FOR  
THREE-PHASE SLURRY REACTORS

**TYPE OF  
REPORT:** Final Report

**PERIOD OF  
PERFORMANCE:** September 1, 1999 to August 31, 2004

**PI:** Goodarz Ahmadi

**DATE  
ISSUED:** June 2003

**GRANT NO.:** DE-FG2699-FT40458

**INSTITUTION:** Clarkson University  
Potsdam, NY 13699-5725  
Tel: (315) 268-2322  
Fax: (315) 268-6438  
Email: ahmadi@clarkson.edu

**STUDENTS:** X. Zhang, W. Chen, A.R. Mazaheri, H. Zhang, C. He, J. Cao

**DOE Project Officers:** Dr. Donald Krastman

## ABSTRACT

In this project, an Eulerian-Lagrangian formulation for analyzing three-phase slurry flows in a bubble column was developed. The approach used an Eulerian analysis of liquid flows in the bubble column, and made use of the Lagrangian trajectory analysis for the bubbles and particle motions. The bubble-bubble and particle-particle collisions are included in the model. The model predictions are compared with the experimental data and good agreement was found.

An experimental setup for studying two-dimensional bubble columns was developed. The multiphase flow conditions in the bubble column were measured using optical image processing and Particle Image Velocimetry techniques (PIV). A simple shear flow device for bubble motion in a constant shear flow field was also developed. The flow conditions in simple shear flow device were studied using PIV method. Concentration and velocity of particles of different sizes near a wall in a duct flow was also measured. The technique of Phase-Doppler anemometry was used in these studies.

An Eulerian volume of fluid (VOF) computational model for the flow condition in the two-dimensional bubble column was also developed. The liquid and bubble motions were analyzed and the results were compared with observed flow patterns in the experimental setup.

Solid-fluid mixture flows in ducts and passages at different angle of orientations were also analyzed. The model predictions were compared with the experimental data and good agreement was found. Gravity chute flows of solid-liquid mixtures were also studied. The simulation results were compared with the experimental data and discussed.

A thermodynamically consistent model for multiphase slurry flows with and without chemical reaction in a state of turbulent motion was developed. The balance laws were obtained and the constitutive laws established.

## TABLE OF CONTENTS

	<b>Page</b>
<b>TITLE PAGE</b>	<b>2</b>
<b>DISCLAIMER</b>	<b>3</b>
<b>ABSTRACT</b>	<b>4</b>
<b>TABLE OF CONTENTS</b>	<b>5</b>
<b>OBJECTIVES</b>	<b>6</b>
<b>SIGNIFICANCE TO FOSSIL ENERGY PROGRAM</b>	<b>6</b>
<b>FINAL REPORT</b>	<b>7</b>
<b>GENERAL</b>	<b>7</b>
<b>HIGHLIGHT OF ACCOMPLISHMENTS</b>	<b>7</b>
<b>EXPERIMENTAL STUDY</b>	<b>9</b>
<b>1. EXPERIMENTAL STUDY OF BUBBLE COLUMN</b>	<b>9</b>
<b>2. SHEAR FLOW EXPERIMENTS</b>	<b>16</b>
<b>COMPUTATIONAL MODELING</b>	<b>28</b>
<b>1. EULERIAN-LAGRANGIAN MODEL FOR         THREE-PHASE SLURRY FLOWS</b>	<b>28</b>
<b>2. TWO-PHASE FLOWS IN A DUCT WITH HEAT TRANSFER</b>	<b>47</b>
<b>3. TWO-PHASE FLOWS IN HORIZONTAL AND INCLINED DUCTS</b>	<b>56</b>
<b>4. EULERIAN VOF ANALYSIS OF BUBBLE COLUMN</b>	<b>61</b>
<b>ARTICLES, PRESENTATIONS AND STUDENT SUPPORT</b>	<b>65</b>

## OBJECTIVES

The general objective of this project is to provide the needed fundamental understanding of three-phase slurry reactors in Fischer-Tropsch (F-T) liquid fuel synthesis. The other main goal is to develop a computational capability for predicting the transport and processing of three-phase coal slurries. The specific objectives are:

- To develop a thermodynamically consistent rate-dependent anisotropic model for multiphase slurry flows with and without chemical reaction for application to coal liquefaction.
- To provide experimental data for phasic fluctuation and mean velocities, as well as the solid volume fraction in the shear flow devices.
- To develop an accurate computational capability incorporating the new rate-dependent and anisotropic model for analyzing reacting and nonreacting slurry flows, and to solve a number of technologically important problems.
- To verify the validity of the developed model by comparing the predicted results with the performed and the available experimental data under idealized conditions.

## SIGNIFICANCE TO FOSSIL ENERGY PROGRAM

Converting coal to liquid hydrocarbon fuel by direct and indirect liquefaction processes has been of great concern to the development of coal-based energy systems. While the direct hydrogenation has been quite successful and was further developed in various forms, use of slurry phase Fischer-Tropsch (F-T) processing is considered a potentially more economical scheme to convert synthesis gas into liquid fuels. Slurry transport and processing and pneumatic transport of particles play a critical role in the operation, efficiency, safety and maintenance of these advanced coal liquefaction and coal-based liquid fuel production systems. Therefore, a fundamental understanding of reacting coal slurries will have a significant impact on the future of environmentally acceptable liquid fuel generation from coal.

Particle-particle and particle-gas/liquid interactions strongly affect the performance of three-phase slurry reactors used in coal conversion processes and are crucial to the further development of coal-based synthetic hydrocarbon fuel production systems. The scientific knowledge base for these processes, however, is in its infancy. Therefore, most current techniques were developed on an *ad hoc* and trial and error basis. This project is concerned with providing the needed fundamental understanding of the dynamics of chemically

active slurries and three-phase mixtures. In particular, a computational model for predicting the behavior of dense mixtures in coal liquefaction and liquid fuel production equipment will be developed.

## **FINAL REPORT**

### **GENERAL**

The highlight of the accomplishment is first summarized. This is followed by the reports of various accomplishment of the project. One important additional accomplishment of the project is the development of an experimental setup for a two-dimensional bubble column. This additional effort, which was not in the scope of the original proposed work, was undertaken to provide quantitative data for our model verification. In addition an Eulerian-Lagrangian computational model for analysis of three phase flows was also developed. This additional important contribution also was not in the scope of the original project.

### **HIGHLIGHT OF ACCOMPLISHMENTS**

An Eulerian-Lagrangian formulation for analyzing three-phase slurry flows in a bubble column was developed. The approach uses an Eulerian analysis of liquid flows in the bubble column, and makes use of the Lagrangian trajectory analysis for the motions of bubbles and particles. The developed method accounts for the two-way interactions of the three-phase flows, including bubble-bubble, particle-particle, and bubble-particle collisions.

A computational model for two-phase flow was developed and the flows in horizontal and inclined ducts were analyzed. The results were compared with the available experimental data and earlier model predictions and good agreements were observed. A computational model for analyzing two-phase solid-liquid flows at various mass loading ratios was also developed and was successfully used to predict flow parameters down an inclined chute.

An experimental set-up for generating a two-dimensional bubble column for detail studies was designed and fabricated. Experimental data for the multiphase flows liquid-gas flow were obtained using optical image processing as well and Particle Image Velocimetry (PIV). In addition an experimental simple shear flow apparatus was developed. The device generate simple shear flow field for range of parameters. Bubbles were injected into the shear flow apparatus and the subsequent motion of the bubbles and the liquid velocity and turbulence intensity were measured using PIV techniques.

Two-phase bubbly flows using the volume-of-fluid (VOF) approach was also studied. The Lagrangian trajectory of a dilute concentration of the solid phase is also studied. In a related

modeling effort, a rate dependent thermodynamically consistent model for slurry flows was developed. The new model includes the effect of phasic interactions and appears to lead to anisotropic effective stress tensor.

We analyzed turbulent two-phase flows with heat transfer. We developed an Eulerian/Lagrangian approach including the two-way interaction for two-phase flows. The model considers the thermal turbulent field characteristics and includes an explicit equation for temperature fluctuation in addition to the turbulence kinetic energy and time scales of the flow and thermal field fluctuations.

We also made in measurements of concentration and velocity profiles of particles of different sizes near a solid wall in a duct flow. The result shows that small particles have diffusion dominated concentration profiles near the wall, while the larger particles could acquire an inertial dominated counter gradient profile.

## EXPERIMENTAL STUDY

### 1. EXPERIMENTAL STUDY OF BUBBLE COLUMN

#### 1.1. Experimental Setup

Two experimental setups for a two-dimensional bubble column is designed and fabricated. One setup is 120 cm high and 15 cm wide with a thickness of 1 cm, and is made of Plexiglas. The gas distributor is made up of eight tube injectors flush mounted on the bottom plate of the column. Each gas injector opening is 1mm, generating an initial bubble size of about 3~8 mm. The distance between two adjacent injectors is 2 cm and that between the end injector and the sidewall is 1 cm. The column in the second setup is 80 cm high and 40 cm wide with a thickness of 1 cm. The spacing between the injector is about 6 cm in this case. In both setups, air flows through each injector individually from a mixing chamber, which is regulated by a flow-meter. The superficial gas velocity ranges from 2 to 20 cm/s. Tap water is used as the liquid phase. The liquid phase is operated under batch condition and the static liquid height is kept constant at 80~100 cm for all runs.

A CCD camera is used to observe the flow conditions in the bubble column and the data is recorded on a computer for analysis. Schematic of the narrow column setup is shown in Figure 22. A sample picture of the bubble dispersion in the column during the experiment can be seen in Figure 23.

#### 1.2. Image Analysis

At a given superficial gas velocity  $U$  and height above the distributor  $h$ , one experimental run consisting of three samples of ten seconds, result in 300 images. The captured images are processed by Labview IMAQ. The first step in the image processing is the conversion of 32 bit images into 8 bit images. Each pixel in the image has a so-called grey value ranging from 0 to 255. A gray value of 0 corresponds to black and gray value of 255 to white. A region of interest is defined by the image with  $540 \times 480$  pixels representing  $0.15 \times 0.10$  m window of observation in column. A typical picture resolution from the first image processing steps is shown in Figure 24 for air bubbles in water.

The next step is segmentation of the images, which subdivides an image into its constituent parts. The most common way is to apply the technique of thresholding. This can be either done by deciding a threshold level or by using the entropy method. Therefore the optimal threshold gray value  $T_h$  lies between the peaks of distribution. For any given coordinate  $(x,y)$  in an image with a gray level  $f(x,y)$ , thresholding operation can be expressed as

$$g(x,y) = \begin{cases} 1 & \text{if } f(x,y) \geq T_h \\ 0 & \text{if } f(x,y) \leq T_h \end{cases} \quad (5-1)$$

where  $g(x,y)$  is the grey level of the corresponding picture in the resulting binary image.

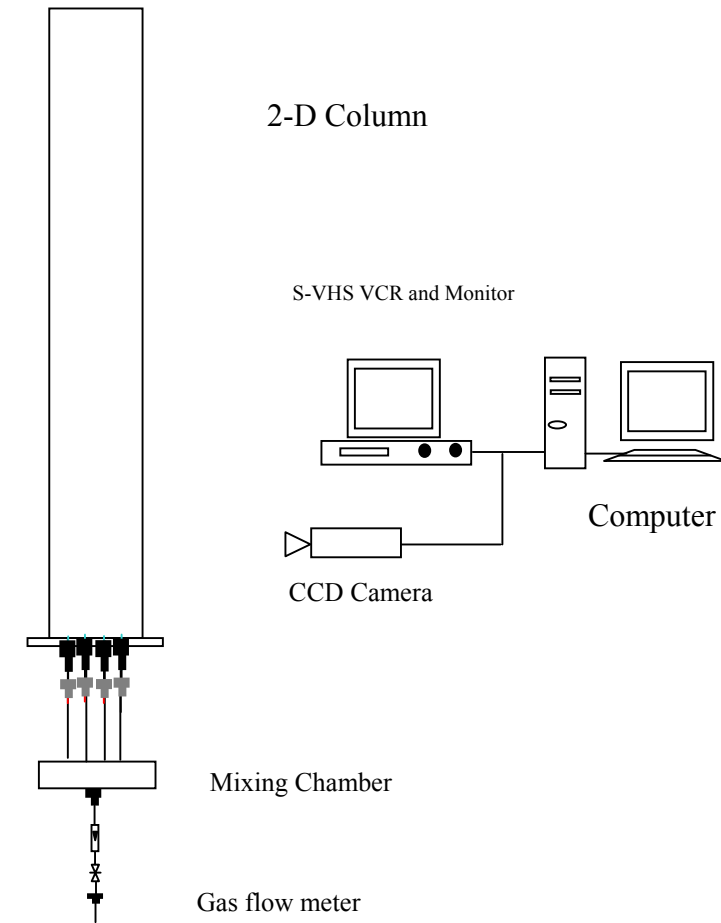


Figure 22. Schematics of the experimental bubble column.



Figure 23. A picture of the bubble dispersion in the bubble column.

Application of this thresholding to Figure 24 results in the binary image. The last step in the image process is the measurement of the shape of each object in the image. Object properties include area, diameter, perimeter, width and height. Present study is focused on the diameter of objects. After completion of the image processing, the number of pixels that form an individual bubble converted into the bubble area,  $A_b$ , then into the bubble diameter,  $d_b$ , using

$$d_b = \sqrt{\frac{4}{\pi} A_b} . \quad (5-2)$$

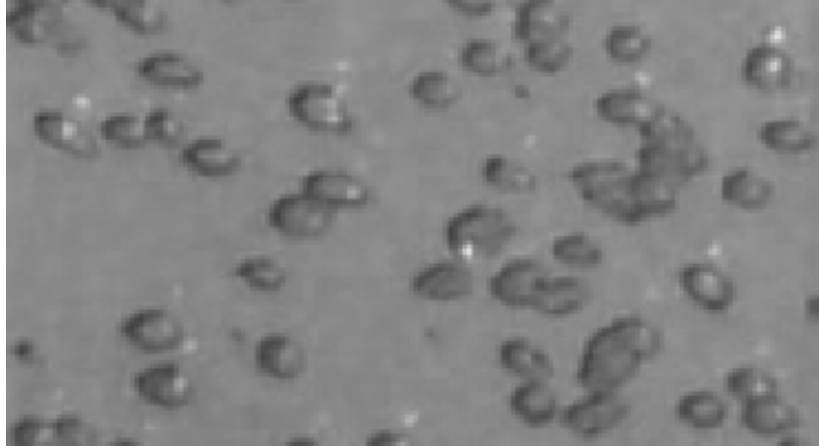


Figure 24. Typical image of bubbles captured by the CCD camera.

The gas hold up in the column can then be evaluated. i.e.,

$$\varepsilon_g = \frac{\sum_1^n \frac{1}{6} \pi \times d_{bi}^3}{V_c}, \quad (5-3)$$

where  $V_c$  represents the volume of the column. The procedure was first calibrated by video imaging objects (circles or squares) of known areas.

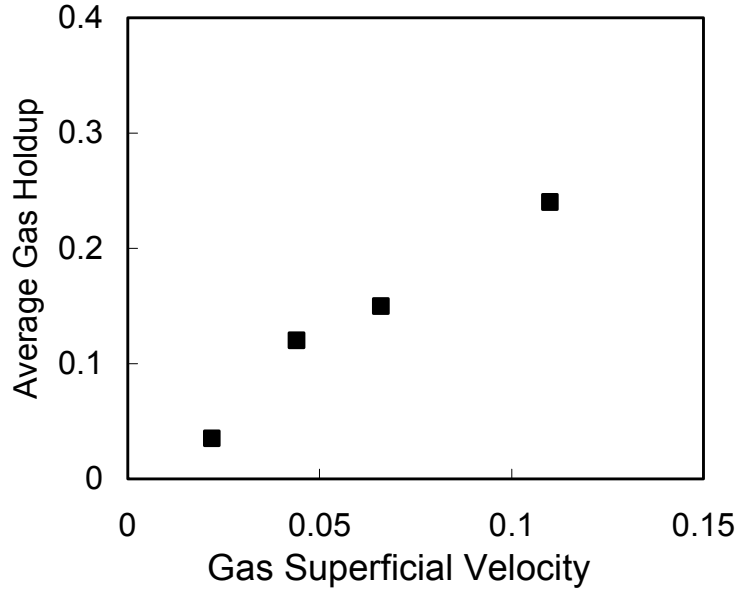
### 1.3. Average gas holdup and its axial profile

Figure 25 shows the effect of superficial gas velocity on the average gas holdup. This figure shows that with the increase of superficial gas velocity, the average gas holdup increases. Increasing the superficial gas velocity leads to formation of larger bubbles and make bubble size distribution shifting toward the larger sizes. The gas holdup is the result of convection of bubbles captured by the liquid flow, in addition to bubble coalescence and breakage process, which in turn depend upon the gas holdup distribution and energy dissipation rate in the column. At lower gas superficial velocities, mean axial upward velocity of liquid is obviously smaller than that at higher gas velocities. The lower mean velocity can offers more residence time for gas bubble before they are released from the column free surface. However, the bubble concentration is also lower. At higher gas velocities, though bubble residence time is less than that at lower gas velocities, and the bubble concentration is much higher. Since more bubble coalescence occurs at higher gas velocity and bubble population shift more towards larger bubble sizes. The observation of shifting of the distribution toward the larger size with increase of superficial velocity is in agreement with most of earlier works.

Axial bubble volumetric concentration profile for gas superficial velocities of 0.02, 0.04 and 0.12 m/s from batch experiments are shown in Figure 26. It is seen that the axial bubble concentration profile in the column is slightly higher at the bottom of the column and decrease

gradually toward the free surface. While the profile is nearly uniform, a slight increase near the free surface is observed. Foam was also observed during these batch experiments.

Effect Superficial Gas Velocity on Average Gas Holdup



Effect of Superficial Gas Velocity on Axial Gas Holdup

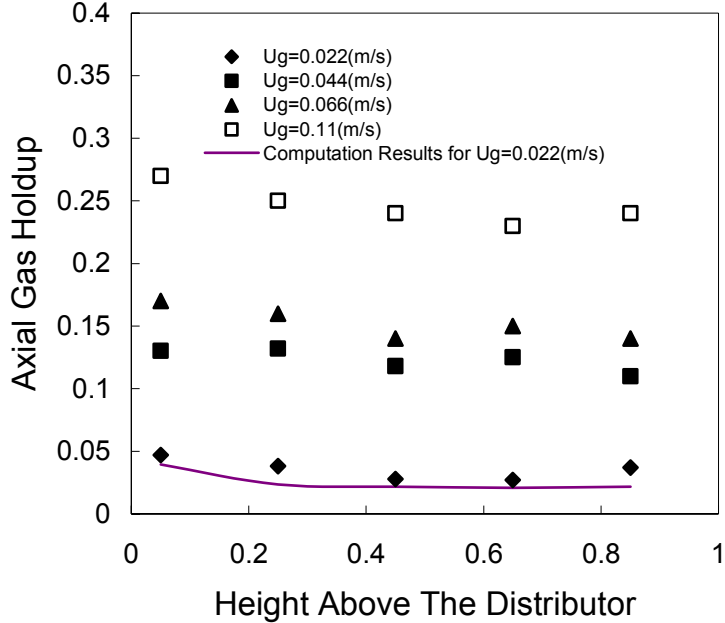


Figure 26. Variations of axial bubble volumetric concentration profiles with superficial gas velocity.

## 1.4. Single Bubble Trajectory

Sample images during the motion of a single bubble are shown in Figure 27. In order to estimate the trajectory of the bubble, the bubble center of mass and orientation need to be defined. The mass center was evaluated using image analysis based on the area of the bubble image. The bubble orientation,  $\theta$ , is defined as the angle between the vector formed by connecting the central point of the bubble to its tip in the projected image and the y axis. This vector is also normal to the flatten bottom surface of the bubble. It was noticed that a bubble moves in a zigzag motion in the bubble column. This irregular motion of the bubble is determined by the interaction of the bubble wake structure and the bubble deformation. The magnitude of the orientation of the bubble to some extent expresses such interactions. Figure 28 shows a typical sample trajectory of a single bubble in the column. The distribution of the bubble orientation in the bubble column is shown in Figure 29. It is seen that the orientation of the bubbles in the observation window falls in the range from  $-40^\circ \sim 40^\circ$ . Here the average size of the bubbles is 5mm. It is expected that the amplitude of the bubble orientation be related to with the period of the bubble oscillation. This point, however, deserves additional studies.

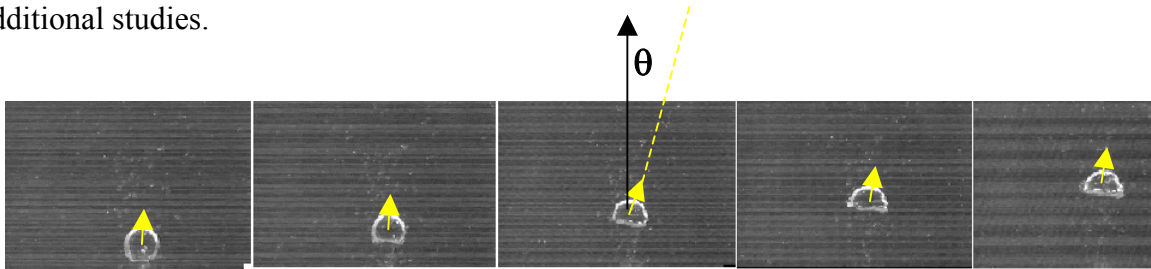


Figure 27. Sample images of a single bubble and definition of bubble angle.

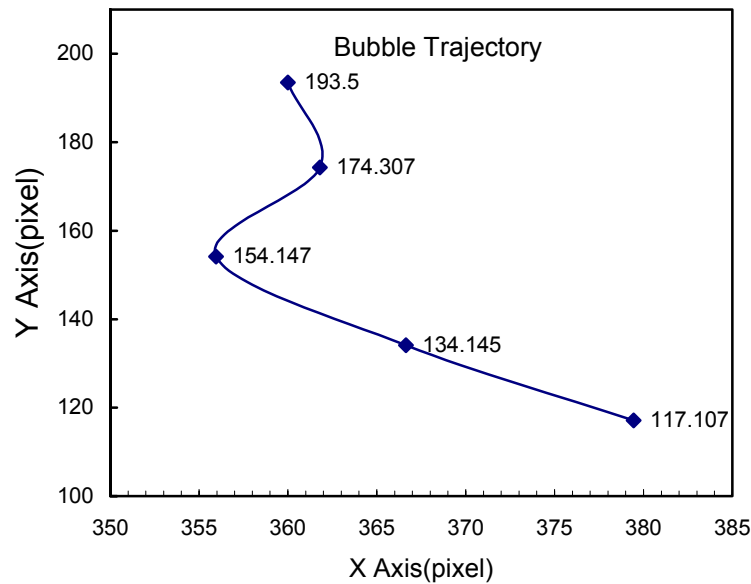


Figure 28. Sample trajectory of a typical bubble in the bubble column.

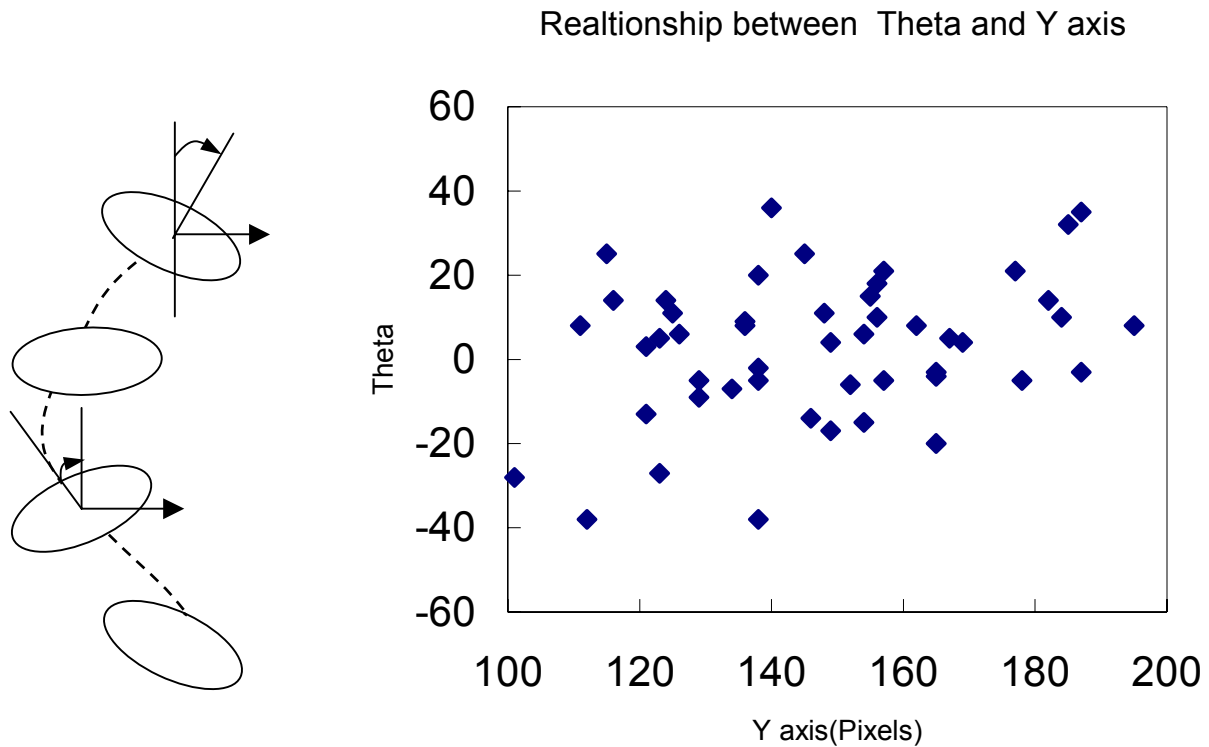


Figure 29. Distribution of bubble orientation measured with respect to the with y

### 1.5 Wide Column Experiments

The second experimental setup for the bubble column is 80 cm high and 40 cm wide with a thickness of 1 cm. This column is also made of Plexiglas. The gas distributor is made up of five tube injectors flush mounted on the bottom plate of the column. Each gas injector opening is 1/8 inch, generating an initial bubble size of about 5~8 mm. The distance between two adjacent injectors is 7 cm and that between the end injector and the sidewall is 6 cm. The superficial gas velocity in the range of 5 to 60 cm/s was used in this study. The liquid phase is operated under batch condition and the static liquid height is kept constant at 70 cm for all runs.

Typical experimental image of bubble plume in the column is shown in Figure 30. Two major circulating flow pattern develops in column. In the center of the column, small bubbles tend to coalesce and merge into larger bubbles. These large bubbles forms the main body of the bubble plume that move upwards in the center of the column. At the top of the column, most bubbles are released at the column free surface. Some bubbles, however, breakup into smaller bubbles due to the interaction with turbulence and shear flow field. These smaller bubbles are captured by the recirculation flow in the column and move back to lower part of the column. The liquid downward flow occurs in the region close to the side walls. Generally the bubbles in the center are bigger and move upwards while the bubbles near the both

walls are smaller and move downwards. The bubble breakup happens in the upper part of the column. The bubble coalescence happens in the lower section. The plume oscillation noted by some authors could not be clearly seen range of operation of the column in the present study. This could be due to the fact that the distributor structure or operation parameters have a significant effect on the generation of the bubble plumes oscillations. In the present work, a uniformly spaced holes was used for air injection form distributor into the column, while other authors used the centered sparger in their experiment.

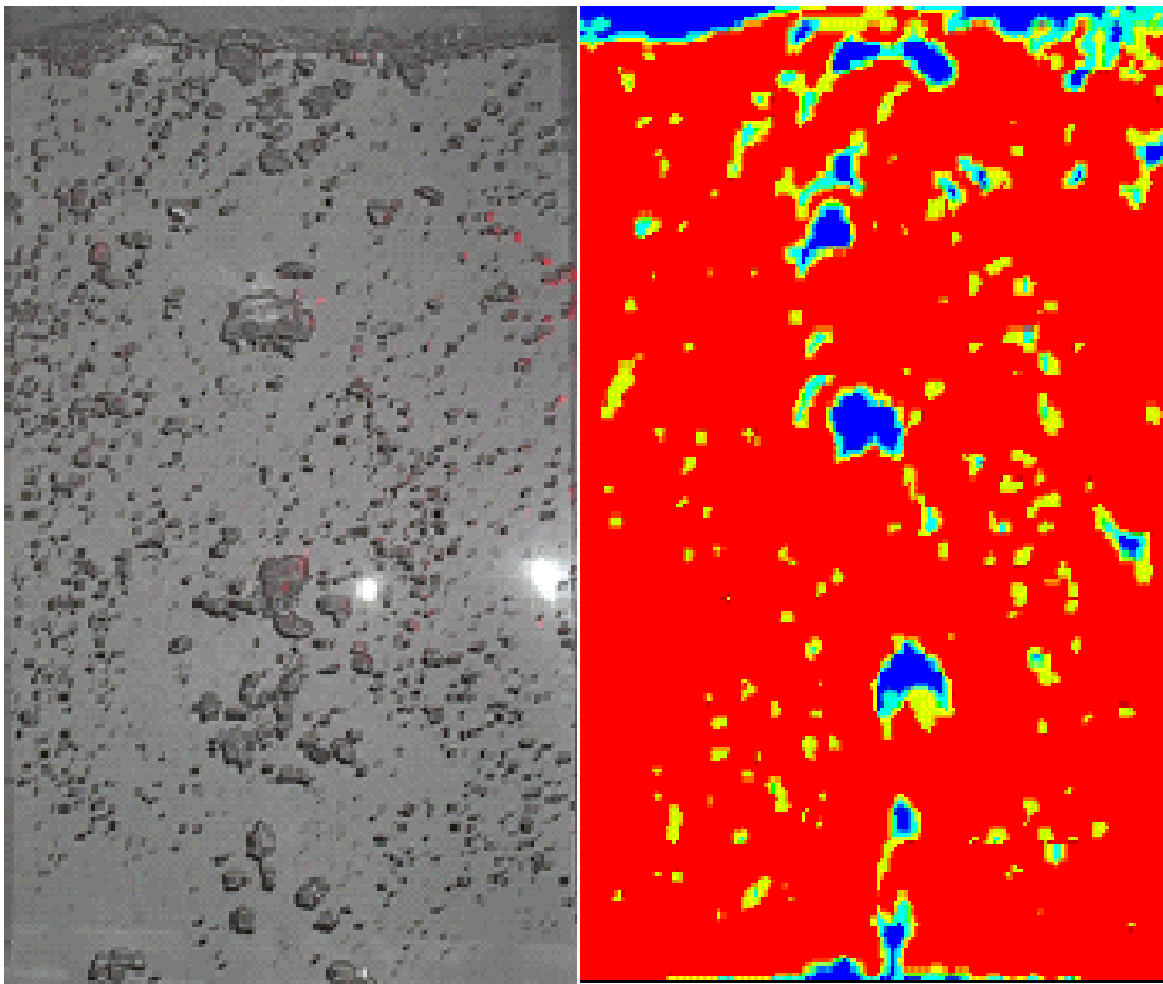


Figure 30. Comparisons between the snapshots of bubble plumes and VOF simulation.

## 2. SHEAR FLOW EXPERIMENTS

### 2.1 Experimental Setup

The experimental set-up consists of a simple shear flow apparatus similar to the one used by Graham and Bird and Cherukat, McLaughlin and Graham and a particle Image Velocimetry (PIV) measurement system. The simple shear flow apparatus was used to produce a linear shear flow field. The apparatus contains two rubber timing belt pass over pulleys with matching pitches that rotate in the same sense. Hence the belts move in opposite directions in the viewing section and generate a simple shear flow condition. The fluid is contained in the space between the two Plexiglas sheets and the aluminum block. A Schematic of the simple shear flow device is shown in Figure 31.

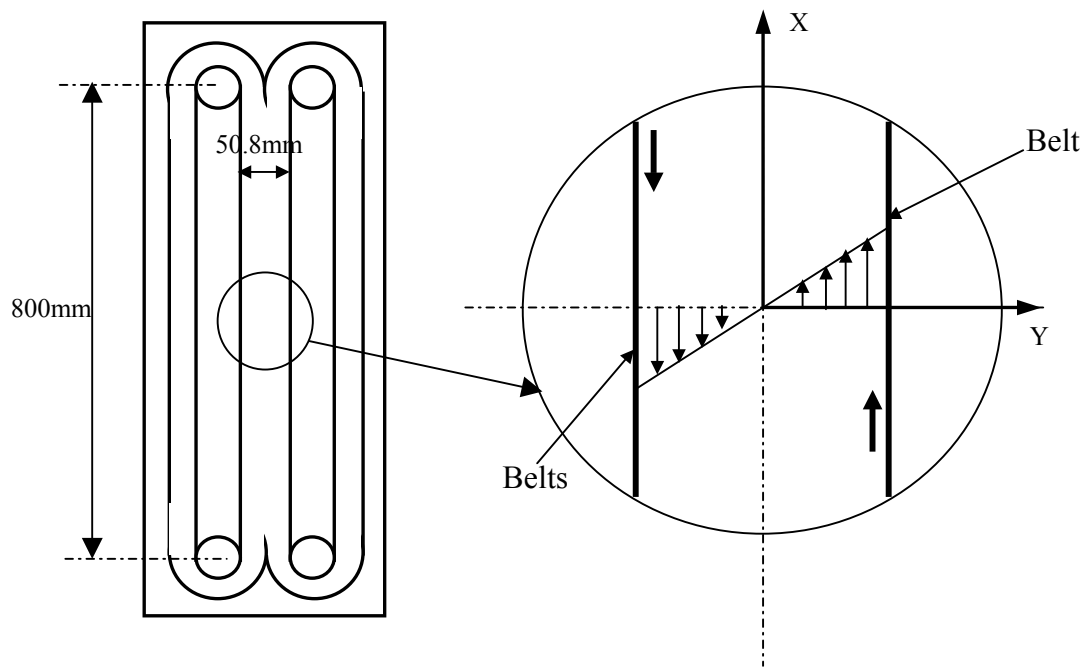


Figure 31. Schematic of the simple shear flow apparatus.

The test window is in the middle of the viewing section. Sprockets are fixed to the shafts attached to the bottom pulley and these are driven by a chain drive attached to a DC motor. The speed of motor is controlled electronically. The gap between the belts is 50.8 mm, and the width of each belt is 101.6 mm. The belts speed is determined by rotation of pulleys that is detected by rotation meter. The characteristics of flow in the apparatus depend on the device Reynolds number, which is defined as

$$Re_e = \frac{V_b b}{2\nu}, \quad (5-4)$$

where  $V_b$  is the belt speed and  $b$  is the gap the between the belts.

## 2.2 Measurement Technique

A DANTEC FLOW MAP 2100 PIV system was used in the experiment which consists a digit camera, an Nd:YAG laser, and a processor. A pair of pulse NEW WAVE RESERCH 120mJ Nd:YAG lasers were used to illuminate a plane normal to the surface of the belts. The laser was pulsed at time separation of 2200  $\mu$ s for the different belt Reynolds numbers. This inter-frame delay was selected to provide ample time for the fastest moving tracer particles to traverse roughly  $\frac{1}{2}$  the width of the interrogation area between frames. When each laser was pulsed a KODAK MEGAPLUS digital camera was triggered and captured a 50.8mm $\times$ 50.8mm image of the seeded flow as it passed through the test window. A schematics of the experimental setup is shown in Figure 32.

The DANTEC processing algorithm partitions each image into a series of 64 $\times$ 64 pixel interrogation areas, applies Gaussian window function to reduce spectral ring, and used a band pass filter to remove erroneous peaks caused by aliasing or variation in laser brightness. The processor than performs a fast two-dimensional cross-correlation between the two associated images. Figure 33 present an example of a 32 $\times$ 32 interrogation areas at two times separated by a time delay  $\Delta t$ . Here an example for illustrating the two sequential images, each particle typically covers 2 to 4 pixels and each interrogation area contains 5 to 20 particle as shown in Figure 33. Computing the two-dimensional cross-correlation between two frames yield a peak shifted from the origin. This shift is converted to a distance and used to compute the velocity. To convert from pixels to a distance the PIV system must be calibrated. That the camera has a fixed number of pixels in each direction (1008 $\times$ 1018) a magnification ratio can be determined. For the set-up shown in Figures 31 and 2 this magnification yields a ratio of 52.7  $\mu$ m per pixel shown in Figure 33.

## 2.3 Experimental Conditions

The belt velocity defines the shear rate used. The following dimensionless parameters can be defined:

$$Re_\gamma = \frac{D_e^2 \gamma_{avg}}{\nu}, \quad E_o = \frac{D_e^2 g \rho_l}{\sigma}, \quad M = \frac{g \mu_1^4}{\rho_l \sigma^3} \quad (5-5)$$

Here  $D_e$  is the bubble equivalent,  $Re_\gamma$  is the Reynolds number,  $E_o$  is Eotvos number and  $M$  is Morton number. In these experiment a range of shear rate  $\gamma_{avg}=1.1$  to  $8.55 \text{ s}^{-1}$  was considered. For an average bubble diameter of  $D_e = 5 \text{ mm}$ , Table 1 shows the range of nondimensional parameters

used in the experiment for air bubbles injected into water under simple shear flow conditions.

Table 1. Experimental Conditions.

$\gamma_{avg}$	$Re_\gamma$	$E_o$	M
1.1~8.6	27.5~215	3.356	$2.519 \times 10^{-11}$

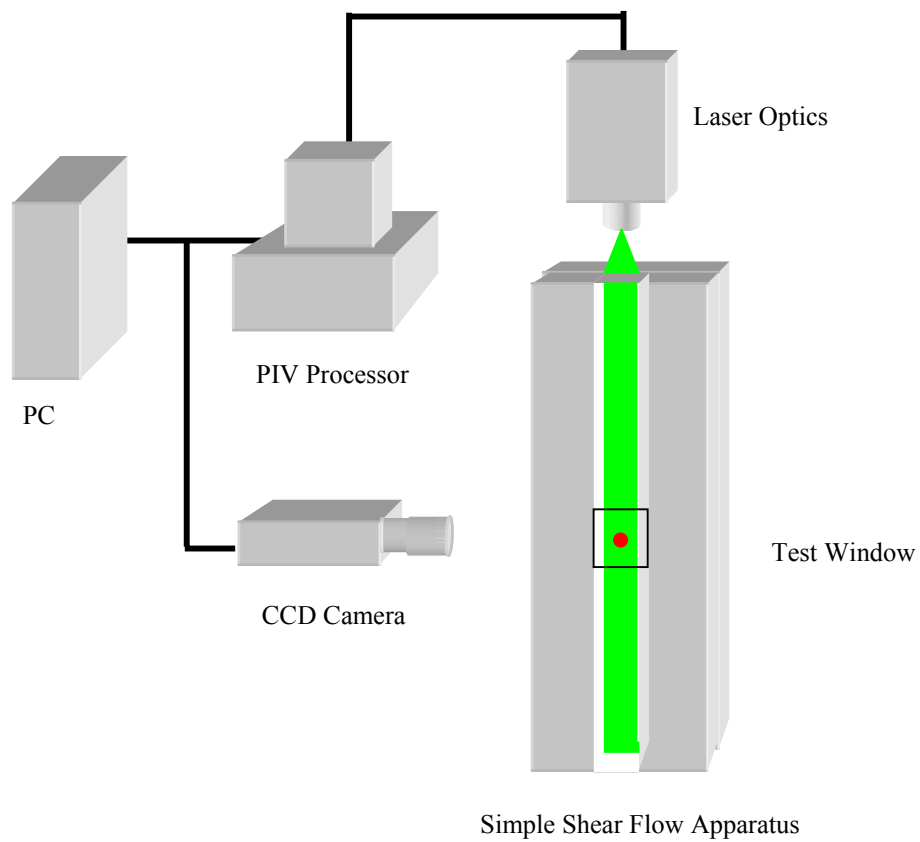


Figure 32. Schematic of measurement setup.

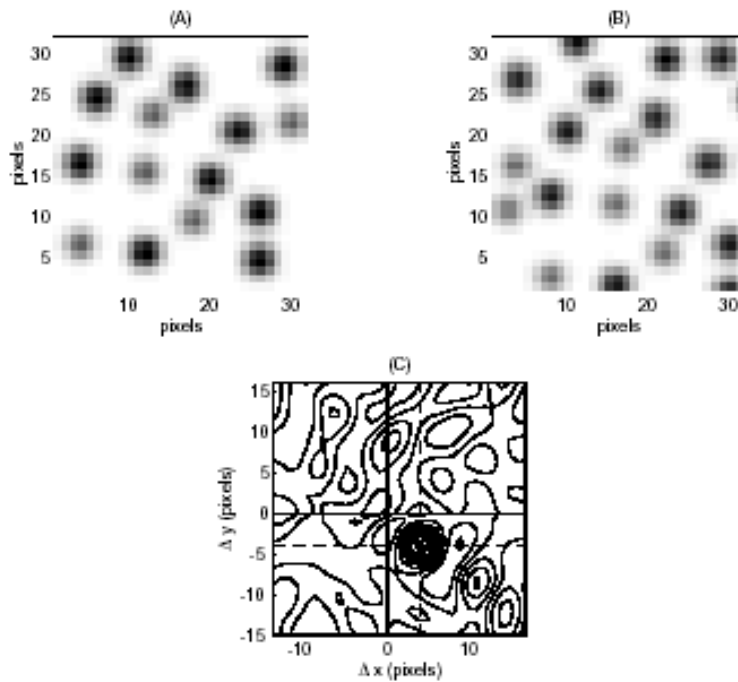


Figure 33. Example of interrogation areas and the cross-correlation between two frames.

## 2.4 Experimental Results

Based on a collection of 265 images the velocity condition in the shear flow device were evaluated. Figures 34-41 show the flow velocity profiles in single phase (liquid) for different shearing velocities.

### 2.4.1 Pure Shear Flow

### 2.4.2 Mean Liquid Velocity Profiles

The mean liquid velocity profiles for range of belt velocities from 0.018 m/s to 0.213 m/s are described in this section. Here  $U$  is the velocity component in the vertical ( $x$ ) direction as shown in Figure 31, and  $V$  is the horizontal component. Figure 34 shows the velocity profiles for a belt velocity of  $U_o = 0.018$  m/s. The computer simulation results are also shown in this figure for comparison. It is seen that the measure velocity profile is nearly linear at this low shearing velocity.

For higher values of belt velocity, the measured and computed velocity profiles are plotted in Figures 35-39. When the belt velocity is larger than 0.04 m/s, the velocity  $U$  profile exhibits two distinct regional variations. Near the walls, the profile is similar to the turbulence boundary layer; while in the core region mean velocity profile is roughly linear. The  $V$ -velocity is expected to be zero for fully developed flows. It, however, shows slight variations across the section that is partly

caused by the vibration of the belt. For belt velocities larger than 0.11 m/s, the U-velocity profiles show some asymmetries that were caused by the vibration of the belts. A close examination of the V-profile also reveals that there were some asymmetric variations which could reach to a peak of about 4% of U.

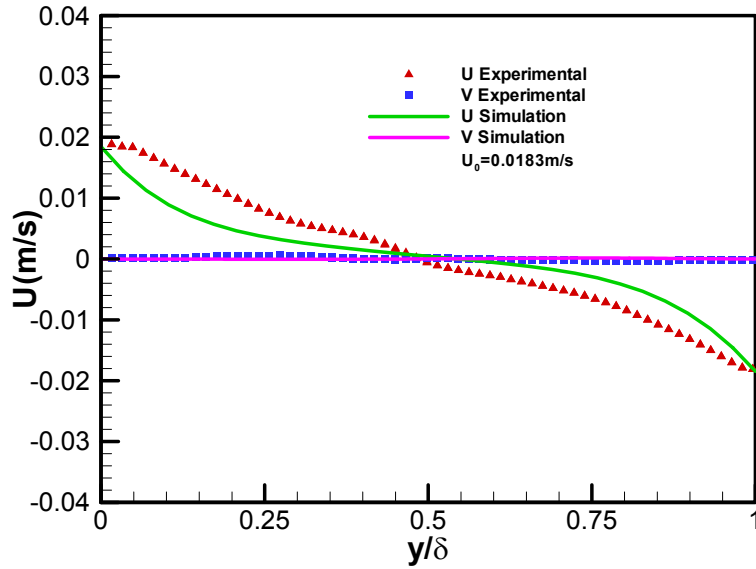


Figure 34. Comparison of the velocity profiles with the simulation results for  $U_0 = 0.018$  m/s.

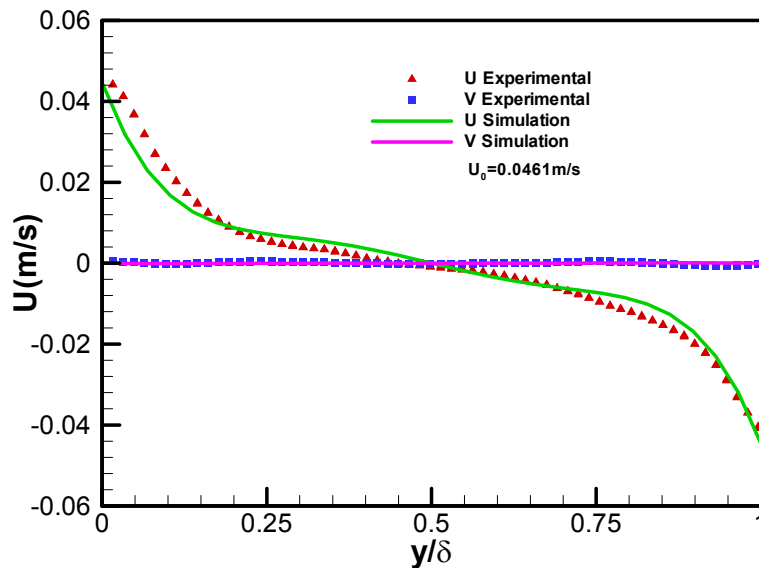


Figure 35. Comparison of the velocity profiles with the simulation results for  $U_0 = 0.046$  m/s.

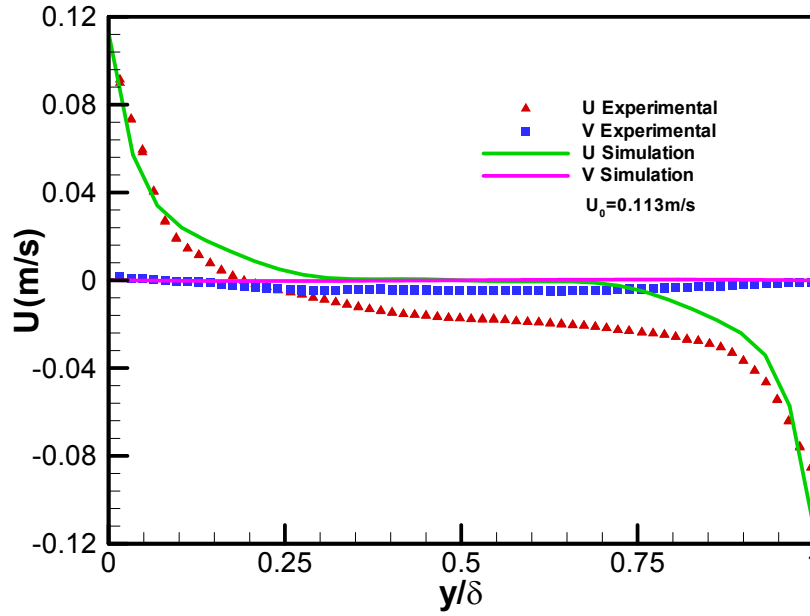


Figure 36. Comparison of the velocity profiles with the simulation results for  $U_0 = 0.113$  m/s.

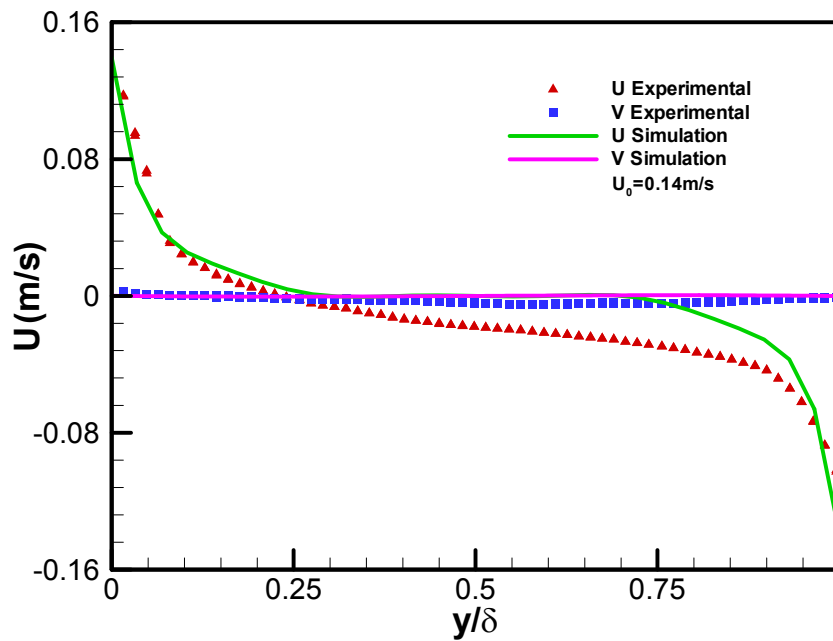


Figure 37. Comparison of the velocity profiles with the simulation results for  $U_0 = 0.14$  m/s.

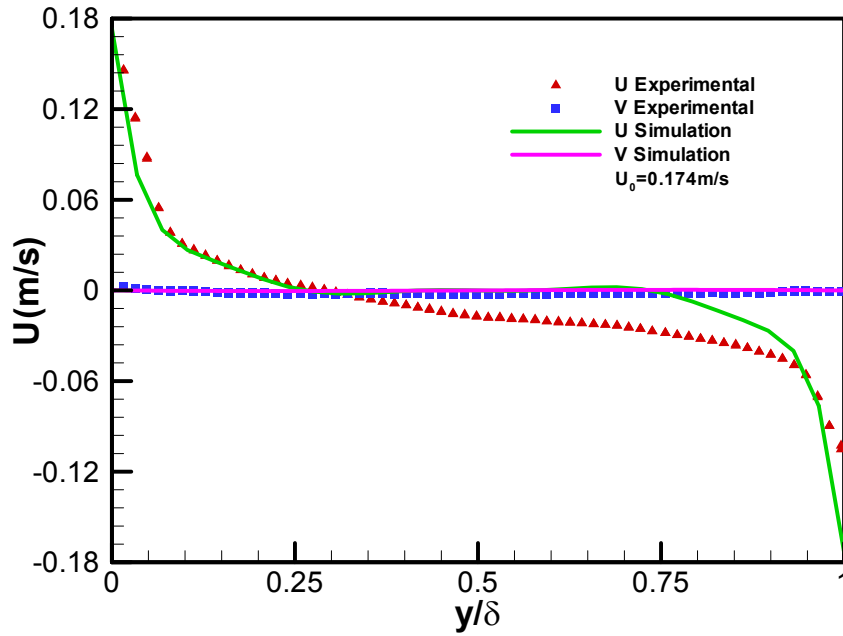


Figure 38. Comparison of the velocity profiles with the simulation results for  $U_0 = 0.17 \text{ m/s}$ .

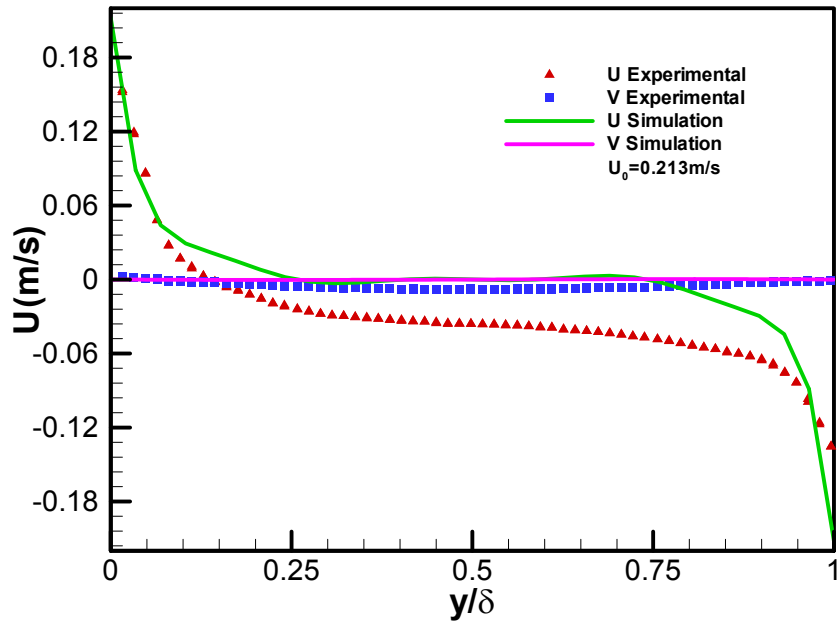


Figure 39. Comparison of the velocity profiles with the simulation results for  $U_0 = 0.213 \text{ m/s}$ .

### 2.4.3 Turbulence Velocities

In this section the measured mean-square turbulence fluctuation velocities  $\overline{u'u'}$ ,  $\overline{v'v'}$ , as well as the cross-correlations  $\overline{u'v'}$  are reported in Figures 40-42. Figure 40 shows the variation of axial mean-square fluctuation velocities for different belt velocities. The intensity is quite high near the wall and decreases toward the centerline as is expected. The profiles for  $\overline{v'v'}$  are shown in Figure 41. Typically, the turbulence intensity in axial direction,  $\overline{u'u'}$ , shown in Figure 40 is much higher than the ones in the y-direction shown in Figure 41. This is because the production of turbulence in shear field is predominantly in the axial component. While the profile for  $\overline{v'v'}$  shows some scatter due to the belt vibrations, the general features is reasonable. The turbulence intensity  $\overline{u'u'}$  and  $\overline{v'v'}$  both increase as the shear rate increases. The variations of turbulence shear stress are shown in Figure 42. It is seen that  $\overline{u'v'}$  is zero at the wall and increases with distance from the wall and peaks at some distance from the wall and then approach a finite value near the centerline. The belt fluctuation, however, resulted in some scatter in the turbulence shear stress data, as well.

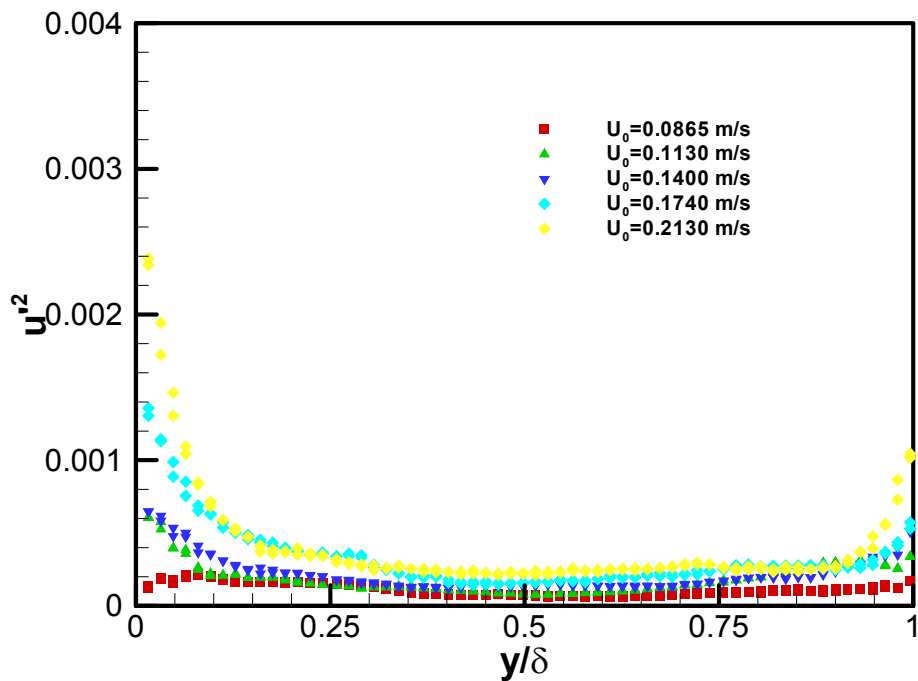


Figure 40. Axial mean-square turbulence intensities profiles for different belt velocities.

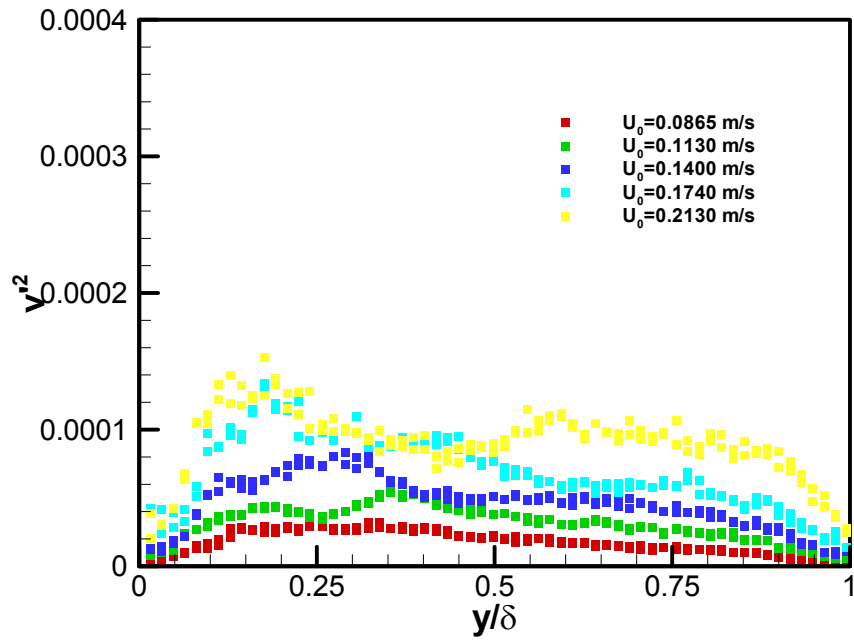


Figure 41. Vertical mean-square turbulence intensities profiles for different belt velocities.

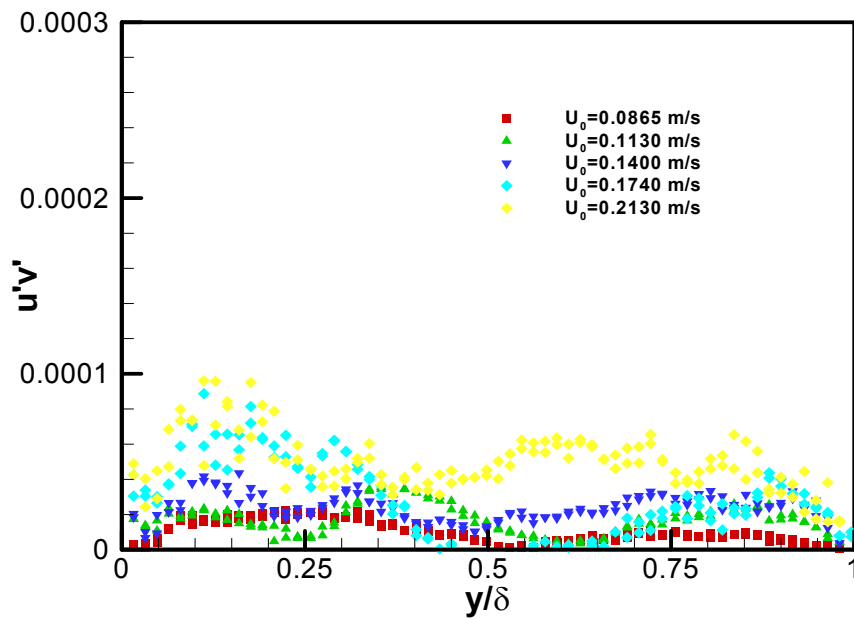


Figure 42. Turbulence shear stress profiles for different belt velocities.

#### 2.4.4 Bubbly Flow in the Shear Device

To study the dynamic properties of bubble motion in shear flow, bubbles are injected from center of the test window as shown in the Figure 32. The bubble sizes are controlled by the diameter of the inject tube and the gas flow rate. Based on the relationship between the initial bubble size and tube diameter, in the present work, the bubble size is kept around 5mm. The bubble injection frequency has a profound effect on the flow field in the shear flow device. Here the bubble injection frequency is varied from zero (no bubble injection) to 6 bubbles per second. The belt velocity was also varied from 0.01 to 0.17 m/s. For every belt velocity, the experiments were repeated for three different bubble injection frequencies. The PIV method was used and the time averaged flow fields were measured. Figures 43 and 44 show the axial velocity ( $U$ ) profiles for different bubble injection frequencies.

The shear flow field is distorted with the injection bubble. It is, however, found that the bubble injection frequency has less effect on the axial velocity profiles for larger shear rates (belt velocity) compared with the cases at the smaller shear rate. For the larger shear velocity of 0.174 m/s shown in Figure 44, it can be seen that the velocity profiles for the different injection frequencies almost lie around the simulation result for the single phase flow. The shear flow field generated by the counter rotating belts dominates the flow fields even though the velocity of the bubble could reach about 20 m/s. Thus, the shearing effect is much large than the bubble drag in this case. While for the smaller shear rate case in Figure 43, the bubble injection affects the flow field profoundly and the effect increase with the bubble injection frequency. Here the  $U$ -velocity profile shows a roughly parabolic shape. That is the bubble drag force comparatively large and distorts the shear flow field.

The corresponding turbulence intensity profiles for the belt velocities of 0.17 m/s and 0.119 m/s, respectively, are shown in Figure 45 and 46. Although the effect of bubble injection frequency on the flow field is different for the different shear rate (belt velocities), it always increases the turbulent intensity. The higher the bubble injection frequencies, the higher turbulent intensity.

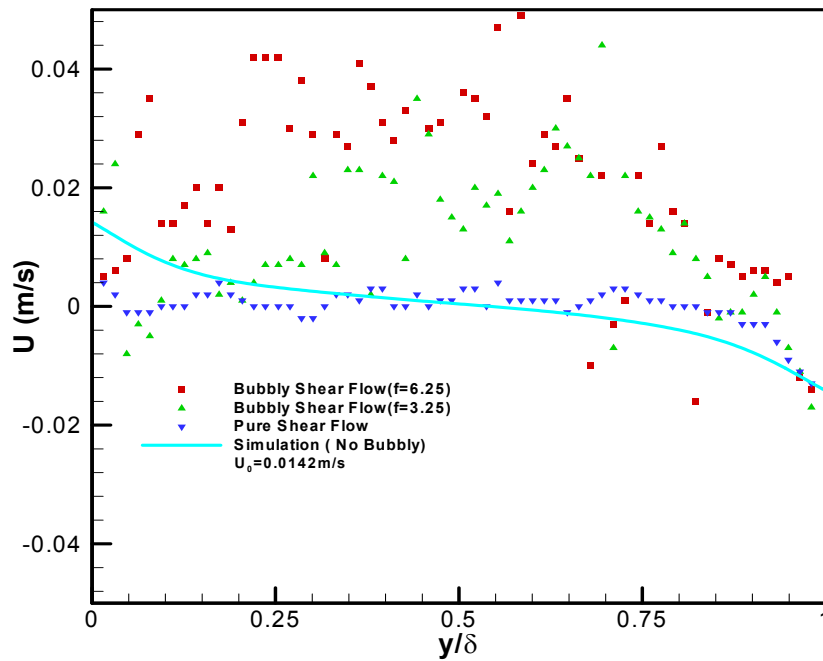


Figure 43. Comparison of the velocity profiles different conditions for  $U_0 = 0.0142$  m/s.

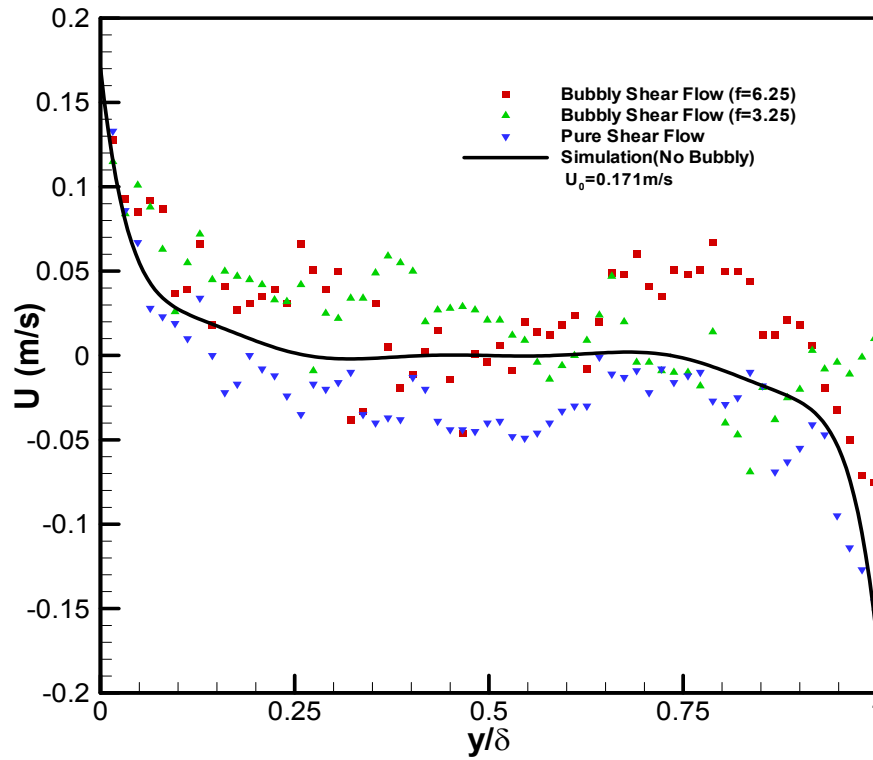


Figure 44. Comparison of the velocity profiles different conditions for  $U_0 = 0.17$  m/s.

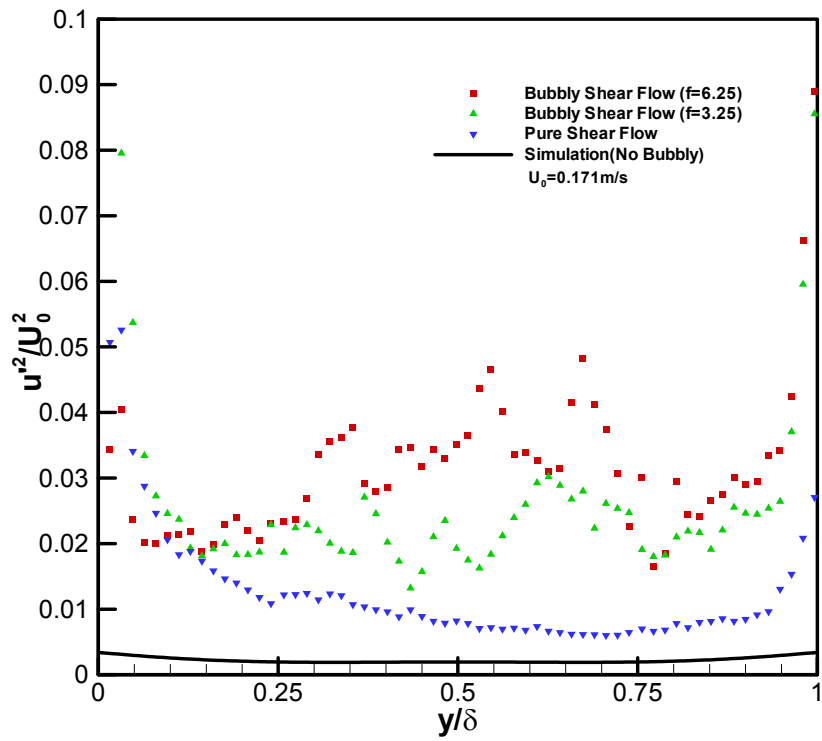


Figure 45. Variations of Turbulence intensity profiles different conditions for  $U_0 = 0.17 \text{ m/s}$ .

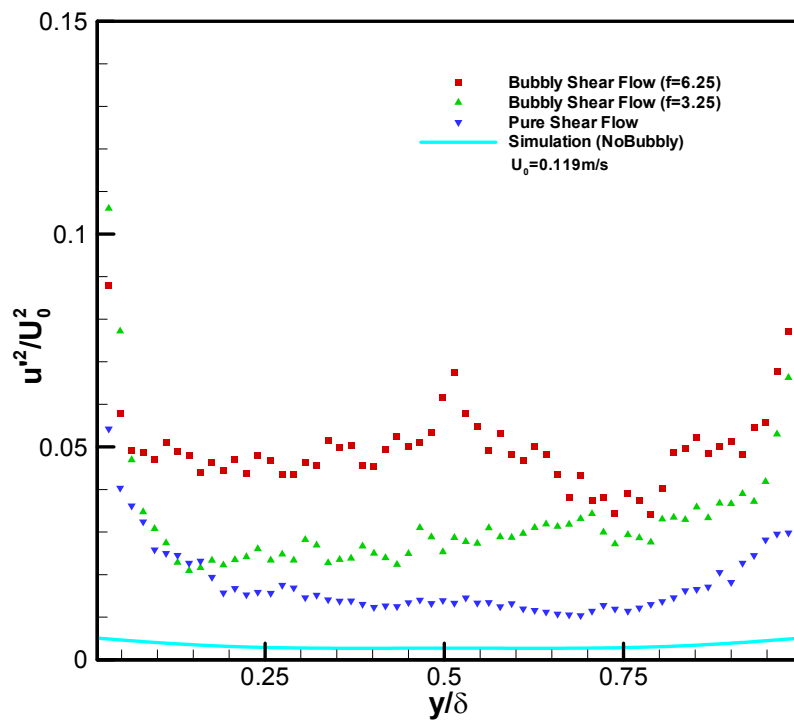


Figure 46. Variations of Turbulence intensity profiles different conditions for  $U_0 = 0.119 \text{ m/s}$ .

## **COMPUTATIONAL MODELING**

### **1. EULERIAN-LAGRANGIAN MODEL FOR THREE-PHASE SLURRY FLOWS**

#### **1.1 Summary**

An Eulerian-Lagrangian computational model for simulations of gas-liquid-solid flows in three-phase slurry reactors is developed. In this approach, the liquid flow is modeled using a volume-averaged system of governing equations, whereas motions of bubbles and particles are evaluated by Lagrangian trajectory analysis procedure. It is assumed that the bubbles remain spherical and their shape variations are neglected. The two-way interactions between bubble-liquid and particle-liquid are included in the analysis. The discrete phase equations include drag, lift, buoyancy, and virtual mass forces. Particle-particle interactions and bubble-bubble interactions are accounted for by the hard particle model approach. The bubble coalescence is also included in the model. The predicted results are compared with the experimental data, and good agreement is obtained. The transient flow characteristics of the three-phase flow are studied and the effects of bubble size on variation of flow characteristics are discussed. The simulations show that the transient characteristics of the three-phase flow in a column are dominated by time-dependent staggered vortices. The bubble plumes move along the S-shape path and exhibit an oscillatory behavior. While particles are mainly located outside the vortices, some bubbles and particles are retained in the vortices. Bubble upward velocities are much larger than both liquid and particle velocities. In the lower part of the column, particle upward velocities are slightly smaller than the liquid velocities, while in the upper part of the column, particle upward velocities are slightly larger. The bubble size significantly affects the characteristics of the three-phase flows and flows with larger bubbles appear to evolve faster.

#### **1.2 Introduction**

Three-phase flows with liquids, bubbles, and solid particles occur in a wide range of industrial processes (Fan, 1989). Important applications include three-phase slurry reactors in coal conversion processes, and in particular, in synthetic liquid fuel production. Optimization of three-phase slurry reactors requires a fundamental understanding of multiphase hydrodynamics coupled with heat and mass transfer processes. Despite a number of investigations on multiphase flows, the three-phase slurry reactor technology is far from being matured with many critical unresolved issues.

There are two main approaches to modeling multiphase flows that account for the interactions between the phases. These are the Eulerian-Eulerian and the Eulerian-Lagrangian approaches. The former is based on the concept of interpenetrating continua, for which all the phases are treated as continuous media with properties analogous to those of a fluid. The Eulerian-Lagrangian approach adopts a continuum description for the liquid phase and tracks the discrete phases using Lagrangian particle trajectory analysis.

In recent years a number of simulation results using Eulerian-Eulerian model were reported in the literature. For gas-particle flows, Sinclair and Jackson (1989) studied gas-particle flows in a

vertical pipe including particle-particle interactions. Ahmadi and Ma (1990) developed a thermodynamical formulation for dispersed multiphase fluid-solid turbulent flows, which was used to study dense simple shear flows (Ma and Ahmadi, 1990). Ding and Gidaspow (1990) developed a bubbling fluidization model using kinetic theory of granular flows. Pita and Sundaresan (1993) performed numerical study on developing flow of a gas-particle mixture in a vertical riser. Abu-Zaid and Ahmadi (1992) proposed a stress transport model for rapid granular flows in a rotating frame of reference. Abu-Zaid and Ahmadi (1996) also developed a rate-dependent model for turbulent flows of dilute and dense two-phase mixtures. Cao and Ahmadi (1995, 2000) reported their numerical simulation results for gas-particle two-phase turbulent flows in vertical, horizontal and inclined ducts. They accounted for the phasic fluctuation energy transport and interactions.

For gas-liquid flows, Gasche et al. (1990) developed a two-fluid model for bubble column reactors. Torvik and Svendsen (1990), Svendsen et al. (1992), and Hillmer et al. (1994) included the effects of turbulence kinetic energy and the dissipation rate caused by the interaction between the two phases in their models. Hjertager and Morud (1993, 1995) treated the liquid and gas phases as space-sharing interdispersed continua and described the interactions through interfacial friction terms. Sokolichin et al. (1993, 1994) reported their simulations using Eulerian-Eulerian method. Krishna et al. (1999) studied the influence of scale on the hydrodynamics of bubble columns using Eulerian-Eulerian model approach and a  $k$ - $\epsilon$  turbulence model. Sanyal et al. (1999) studied gas-liquid flows in a cylindrical bubble column using Eulerian-Eulerian approach and compared their result with algebraic slip mixture model. Borchers et al. (1999) discussed the applicability of the standard  $k$ - $\epsilon$  turbulence model in an Eulerian-Eulerian approach for simulation of bubble columns. Mudde and Simonin (1999) reported their two- and three-dimensional simulation of a meandering bubble plume using Eulerian-Eulerian method that included the  $k$ - $\epsilon$  turbulence model. Additional progress in simulating bubble columns were reported by Rande (1992), Grienberger and Hofman (1992), Boisson and Malin (1996), and Pflieger et al. (1999).

The accuracy of Eulerian-Eulerian approach heavily relies on the empirical constitutive equations used. Furthermore, the approach has limitations in predicting certain discrete flow characteristics. For example, particle size effect, particle agglomeration or bubble coalescence and breakage cannot be fully accounted for. The Eulerian-Lagrangian model, however, involves smaller number of empirical equations and is more suitable for providing detailed information of discrete phases. The disadvantage of this approach is its requirement for more extensive computing time.

The Eulerian-Lagrangian model has been widely used in two-phase flows. Li and Ahmadi (1992), and Kvasnak and Ahmadi (1996) simulated the instantaneous turbulent velocity field across channels and ducts using an anisotropic Gaussian random field model. Sommerfeld and Zivkovic (1992) reported a simulation of pneumatic conveying through pipe systems, in which they incorporated their particle-wall and particle-particle collision models. Using a model described by Crowe (1977), Fan et al. (1997) performed numerical simulations of gas-particle two-phase turbulent flows in a vertical pipe. Tsuji et al. (1993) provided a discrete particle simulation of two-dimensional fluidized bed using a soft particle model. Their model was further modified by

Hoomans et al. (1996) and Xu and Yu (1997) who developed hard sphere collision models. Andrews and O'Rourke (1996), Snider et al. (1998) reported a multiphase particle-in-cell method for dense particulate flows. Zhang (1998) conducted a simulation of gas-particle flows in curved ducts using particle-wall and particle-particle random impact models. Patankar and Joseph (2001a,b) performed simulations of particulate flows using a Chorin-type fractional-step method for gas phase equations. Fan et al. (2001) reported simulations of particle dispersion in a three-dimensional temporal mixing layer. They found that the particle dispersion patterns were governed by the large-scale vortex structures.

Early works based on Eulerian-Lagrangian simulation models for bubbly flows include those of Webb et al. (1992), Trapp and Mortensen (1993), Lapin and Lubbert (1994), and Devanathan et al. (1995). Sokolichin et al. (1996) compared the simulation results of Eulerian-Eulerian model and Eulerian-Lagrangian model with the experimental data, but neglected bubble-bubble interactions. Delnoij et al. (1997a,b) developed an Eulerian-Lagrangian model for a bubble column operating in the homogeneous flow regime. Their simulations incorporated bubble-bubble interactions using a collision model, but ignored bubble coalescence. Lain et al. (1999) developed an Eulerian-Lagrangian approach including turbulence using the  $k - \varepsilon$  turbulence model. Their model, however, neglected the effect of phase volume fractions. More recently, ignoring bubble-bubble interactions, Lapin et al. (2002) reported their Eulerian-Lagrangian simulations of slender bubble columns. Their prediction suggests that the flow moves downwards near the axis and rises close to the wall in the lower part of the column, but in the upper part the opposite trend is observed.

While there is an extensive literature of two-phase flow model, studies of three phase flow hydrodynamics are rather limited. Gidaspow et al. (1994) described a model for three-phase-slurry hydrodynamics. Grevskott et al. (1996) developed a two-fluid model for three-phase bubble columns in cylindrical coordinates. They used a  $k - \varepsilon$  turbulence model and included bubble-generated turbulence. Mitra-Majumdar et al. (1997) proposed a computational fluid dynamic (CFD) model for examining the structure of three-phase flows through a vertical column. They suggested new correlations for the drag between the liquid and the bubbles and accounted for the particle effects on bubble motions. Recently Wu and Gidaspow (2000) reported their simulation results for gas-liquid-slurry bubble column using the kinetic theory of granular flows for particle collisions. Padijal et al. (2000) performed simulations of three-phase flows in a three-dimensional draft-tube bubble column using a finite-volume technique. Gamwo et al. (2003) reported a CFD model for chemically active three-phase slurry reactor for methanol synthesis. However, all these models were based on Eulerian-Eulerian approach. Computer simulations of gas-liquid-solid flows using an Eulerian-Lagrangian model are rather limited. Only recently Zhang (1999) performed a series of simulations of three-phase flow using volume-of-fluid (VOF) method for the liquid and the gas phases and a Lagrangian method for particles. Their study, however, were limited to consideration of only a small number of bubbles.

In this study a detailed Eulerian-Lagrangian model for liquid-gas-solid flows in three-phase slurry reactors is developed. In this model, the liquid is the continuous phase, and the bubbles and particles are treated as the dispersed discrete phases. The small bubbles are assumed to remain

spherical and their shape variations are neglected. The volume averaged, incompressible, transient Navier-Stokes equation is solved for the liquid phase. The bubble and particle motions are simulated by the Lagrangian trajectory analysis procedure. Two-way coupling momentum exchange between the liquid phase and the bubbles and particles are accounted for in the continuous phase momentum equation. Forces acting on the dispersed phases include drag, lift, buoyancy, and virtual mass. A finite difference method is used to discretize the liquid phase equations on a structured equidistant grid. The discrete phase equations are solved with the Runge-Kutta and the Euler methods, for particles and bubbles, respectively. In addition to considering the interactions between particle-particle, bubble-bubble, and particle-bubble, bubble coalescence is also included. The simulation results are compared with the experimental data of Delnoij et al. (1997a) and good agreement was observed.

### 1.3 Governing Equations and Models

#### 1.3.1 Fluid Phase Hydrodynamics

The liquid phase is described by volume averaged, incompressible, transient Navier-Stokes equations. The volume-averaged continuity equation and momentum equation are given by

$$\frac{\partial(\varepsilon_f \rho_f)}{\partial t} + \nabla \cdot (\varepsilon_f \rho_f \mathbf{u}_f) = 0 \quad (1-1)$$

and:

$$\rho_f \varepsilon_f \frac{d(\mathbf{u}_f)}{dt} = -\varepsilon_f \nabla p + \nabla \cdot (\varepsilon_f \boldsymbol{\tau}_f) + \rho_f \mathbf{g} \varepsilon_f + \mathbf{P} \quad (1-2)$$

where  $\varepsilon_f$  is the liquid phase volume fraction,  $\rho_f$  is the liquid phase density,  $\mathbf{u}_f$  is the fluid phase average velocity,  $p$  is pressure,  $\mathbf{g}$  is the acceleration of gravity,  $\mathbf{P}$  is interaction momentum per unit mass transferred from the discrete phases, and  $\boldsymbol{\tau}_f$  is the liquid phase viscous stress tensor, which is assumed to obey the general Newtonian fluid form given as

$$\boldsymbol{\tau}_f = -\frac{2}{3} \mu_f (\nabla \cdot \mathbf{u}_f) \mathbf{I} + \mu_f ((\nabla \mathbf{u}_f) + (\nabla \mathbf{u}_f)^T) \quad (1-3)$$

where  $\mu_f$  is the liquid viscosity.

The volume fraction,  $\varepsilon_f$ , is defined as:

$$\varepsilon_f = (V_{\text{cell}} - V_d) / V_{\text{cell}} \quad (1-4)$$

where  $V_d$  is the volume occupied by the discrete phases and  $V_{cell}$  is the volume of the grid cell given as

$$V_{cell} = dx dy dz \quad (1-5)$$

where  $dx$ ,  $dy$ , and  $dz$  are grid size in  $x$ ,  $y$ , and  $z$  direction, respectively.

### 1.3.2 Dispersed Phase Dynamics

The bubbles and particles are treated as discrete phases and their motions are governed by Newton's second law. i.e.,

$$m_d \frac{d\mathbf{u}_d}{dt} = \mathbf{F}_d + \mathbf{F}_b + \mathbf{F}_{vm} + \mathbf{F}_l + \mathbf{F}_{int} \quad (1-6)$$

where  $\mathbf{u}_d$  and  $m_d$  are, respectively, the discrete phase velocity and mass. The terms on the right hand side of Equation (1-6) are, respectively, drag, buoyancy, virtual mass, lift and interaction forces. Here the interaction force  $\mathbf{F}_{int}$  includes particle-particle, bubble-bubble and particle-bubble collisions.

The drag force,  $\mathbf{F}_d$ , is given by

$$\mathbf{F}_d = \begin{cases} 0.125\rho_f C_D \pi d_d^2 |\mathbf{u}_f - \mathbf{u}_d| (\mathbf{u}_f - \mathbf{u}_d), & Re_d \geq 1 \\ \alpha_d \pi \mu_f d_d (\mathbf{u}_f - \mathbf{u}_d), & Re_d < 1 \end{cases} \quad (1-7)$$

Here  $d_d$  is the discrete phase diameter,  $\alpha_d$  is a phase coefficient whose value is 2 for bubble and 3 for rigid particle to account for the variation of the Stokes drag force for bubbles and particles in low Reynolds number flows. ( $\alpha_d$  is used only when  $Re_d$  is smaller than 1.) In Equation (1-7),  $Re_d$  is the discrete phase Reynolds number defined as

$$Re_d = \rho_f d_d \frac{|\mathbf{u}_f - \mathbf{u}_d|}{\mu_f}, \quad (1-8)$$

and  $C_D$  is the drag coefficient given as

$$C_D = f_d \frac{24}{Re_d}, \quad (1-9)$$

where  $f_d$  is given by

$$f_d = \begin{cases} 1 + 0.15 \text{Re}_d^{0.687}, & \text{Re}_d \leq 1000 \\ 0.0183 \text{Re}_d, & \text{Re}_d > 1000 \end{cases} \quad (1-10)$$

In Equation (1-6),  $\mathbf{F}_l$  is the Saffman lift force given as

$$\mathbf{F}_l = 1.61d_d^2(\mu_f\rho_f)^{0.5}|\boldsymbol{\omega}_f|^{-0.5}[(\mathbf{u}_f - \mathbf{u}_d) \times \boldsymbol{\omega}_f], \quad (1-11)$$

where flow vorticity  $\boldsymbol{\omega}_f$  is defined as

$$\boldsymbol{\omega}_f = \nabla \times \mathbf{u}_f. \quad (1-12)$$

In Equation (1-6),  $\mathbf{F}_b$  is the buoyancy force given by:

$$\mathbf{F}_b = \frac{\pi d_d^3}{6}(\rho_f - \rho_d)\mathbf{g}, \quad (1-13)$$

where  $\rho_d$  is the discrete phase density.

In Equation (1-6),  $\mathbf{F}_{vm}$  is the virtual mass force given by

$$\mathbf{F}_{vm} = -\frac{1}{12}\pi d_d^3\rho_f \frac{d}{dt}(\mathbf{u}_d - \mathbf{u}_f). \quad (1-14)$$

### 1.3.3 Bubble-Bubble and Particle-Particle Collisions

Bubble-bubble and particle-particle collisions are included in this study using a hard sphere collision model along the line of the model developed by Hoomans et al. (1996). The effects of the rotation of bubbles and particles, however, were neglected. Assume all the bubble-bubble and particle-particle collisions are binary collisions, and a and b are discrete phase collision pairs where both can be bubbles or solid particles, the velocities of a and b after a collision are given as

$$\mathbf{u}_{a2} = \frac{p_x}{m_a} + \mathbf{u}_{a1}, \quad \mathbf{v}_{a2} = \frac{p_y}{m_a} + \mathbf{v}_{a1}, \quad (1-15)$$

$$\mathbf{u}_{b2} = \frac{p_x}{m_b} + \mathbf{u}_{b1}, \quad \mathbf{v}_{b2} = \frac{p_y}{m_b} + \mathbf{v}_{b1}. \quad (1-16)$$

where u and v are components of velocity and subscript 1 and 2 refers, respectively, to before and after collision. In Equations (1-15) and (1-16),  $p_x$  and  $p_y$  are the tangential and normal components

of the impulse and, respectively, are given by

$$p_x = \begin{cases} -\mu p_y \operatorname{sgn}(u_{a1} - u_{b1}) & \text{(For sliding case)} \\ -(u_{a1} - u_{b1})/B & \text{(For stick case)} \end{cases}, \quad (1-17)$$

$$p_y = -\frac{(1+e)(v_{a1} - v_{b1})}{C}. \quad (1-18)$$

Here  $e$  is the restitution coefficient,  $\mu$  is the friction coefficient,  $B$  and  $C$  are collision constants given as

$$B = \frac{1}{m_a} + \frac{1}{m_b} + \frac{R_a^2}{I_a} + \frac{R_b^2}{I_b}, \quad C = \frac{1}{m_a} + \frac{1}{m_b}, \quad (1-19)$$

where  $R_a$  and  $R_b$  are, respectively, the radii of particles  $a$  and  $b$ , and  $I_a$  and  $I_b$  are the corresponding moments of inertia given by

$$I_a = \frac{2}{5} m_a R_a^2, \quad I_b = \frac{2}{5} m_b R_b^2. \quad (1-20)$$

The slip and stick conditions during the collision is determined according to

$$\begin{cases} |u_{a1} - u_{b1}| \geq \mu B p_y & \text{(sliding)} \\ |u_{a1} - u_{b1}| < \mu B p_y & \text{(sticking)} \end{cases} \quad (1-21)$$

In the analysis, restitution coefficients of 0.2 and 0.5 are, respectively, used for bubble-bubble and particle-particle collision. Friction coefficients of 0.02 and 0.1 are assumed for bubbles and particles.

Tsao and Koch (1997) reported that the critical Weber number of coalescence for a rising bubble and a stationary bubble is 1.6, and the two bubbles coalesce upon impact at Weber numbers below this value and bounce at higher Weber numbers. Duineveld (1994), however, reported a critical Weber number of 0.18 for the coalescence of two adjacent bubbles based on the relative velocities. Tsao and Koch (1997) suggested that this difference is the result of the major differences in the flow fields. For Duineveld's case, the two bubbles rise side by side, the bubble deformation and fluid flow in the film between the two bubbles may have significant effects on the criterion for coalescence or bouncing. In the present analysis, there are thousands of bubbles in the column that are generally moving side by side. The flow in the bubble column is much more complicated and is expected to have larger effects on bubble-bubble collision process. In the present simulation, bubble coalescence is accounted by assuming that two bubbles coalesce upon impact when the Weber number less than 0.14, while they bounce for larger Weber numbers. Here the Weber number  $We$  is defined as

$$We = \frac{d_b U_b^2 \rho_f}{\gamma}, \quad (1-22)$$

where  $d_b$  is bubble diameter,  $U_b$  is bubble relative velocity,  $\rho_f$  is liquid density,  $\gamma$  is the surface tension.

### 1.3.4 Bubble-Particle Interactions

Bubble-particle interactions are included in the analysis by assuming the particles always go through the bubbles when bubble-particle collision occurs. The particle environment fluid property parameters are then changed from liquid to gas parameters until the particles leave the bubbles. Unlike bubble-bubble and particle-particle encounters, which are assumed to be binary collisions, multi-interactions between bubble and particle are accounted for in this model, which means at the same time, many particles can enter the same bubble or different bubbles.

### 1.3.5 Coupling between Phases

Two-way coupling is included in the model. The coupling between bubbles and particles is implemented through bubble-particle interactions. When a particle enters a bubble, all the forces acting on the particles by the new gaseous environment are calculated using the bubble hydrodynamic properties. The exact force with opposite direction is then added to the bubble equation of motion.

The coupling between fluid and dispersed phases is implemented through momentum interaction term,  $\mathbf{P}$ , from the discrete phase to fluid phase.  $\mathbf{P}$  is the negative of the sum of all forces acting on the particles and bubbles exerted by the fluid in a certain Eulerian cell.

### 1.3.6 Eulerian to Lagrangian and Lagrangian to Eulerian Gridmapping

Liquid phase velocities and pressure from Eulerian approach are evaluated at the face and center of the staggered grids, respectively. However, for calculating the forces acting on the bubbles and particles, the liquid velocities at the locations of bubbles and particles must be evaluated by certain interpolation technique. On the other hand, the forces acting from the bubbles and particles on the liquid phase are exerted at the bubble and particle position. To account for two-way interactions in the computation of the liquid phase motion, an interpolation technique is needed to transfer these forces onto the staggered computational grids. Here an area averaged interpolation scheme for Eulerian to Lagrangian Gridmapping is used. i.e.,

$$\phi_L = \frac{1}{dx dy} [\phi_{E1} A_3 + \phi_{E2} A_4 + \phi_{E3} A_1 + \phi_{E4} A_2], \quad (1-23)$$

where,  $\phi_L$  is the estimated local liquid velocity for the Lagrangian approach,  $\phi_{E1} \sim \phi_{E4}$  are liquid velocities at the grid nodes of the Eulerian frame, and  $A_1 \sim A_4$  are areas of cell fractions shown in Figure 1.

The interpolation scheme used for Lagrangian to Eulerian Gridmapping reads

$$\phi_{E1} = \frac{\phi_L A_3}{dxdy}, \quad \phi_{E2} = \frac{\phi_L A_4}{dxdy}, \quad \phi_{E3} = \frac{\phi_L A_1}{dxdy}, \quad \phi_{E4} = \frac{\phi_L A_2}{dxdy}, \quad (1-24)$$

where,  $\phi_L$  is the force acting on the bubbles and particles in the Lagrangian frame, and  $\phi_{E1} \sim \phi_{E4}$  are the transmitted forces to the Eulerian grid nodes.

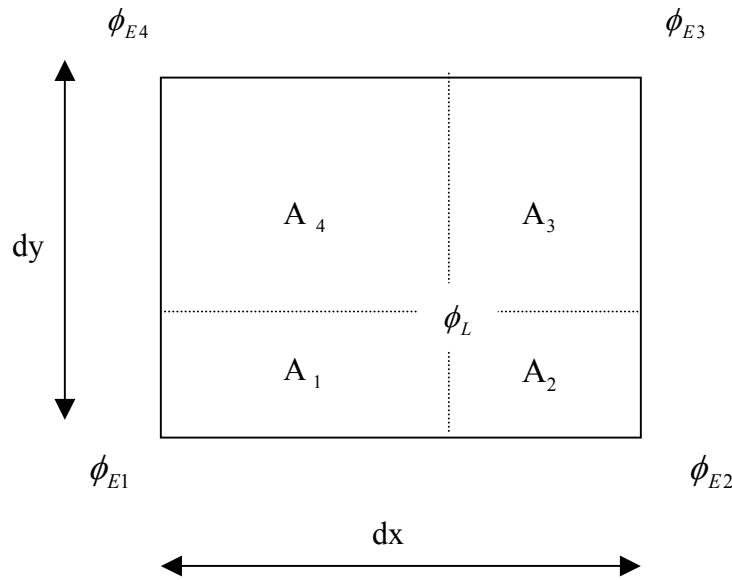


Figure 1. Interpolation scheme from Eulerian to Lagrangian and vice versa.

### 1.3.7 Geometry and Boundary Conditions

The present computational study was focused on a pseudo-two-dimensional bubble column with rectangular cross-section. Figure 2 shows the schematics of the bubble column, which was experimentally studied by Delnoij et al. (1997a). In their setup, bubbles raised through a 25cm wide, 130cm high and 2cm thick column from 14 uniformly spaced gas inlets located in the center of the column bottom surface. The distance between every two neighboring inlet was 4mm. In the simulations, identical geometry was used and neutrally buoyant particles were randomly distributed in the column at the initial time. Similar to the experiment, the continuous phase was assumed to be liquid water. The physical properties of water were kept fixed in the simulations, while the height of liquid level and the properties of particles and bubbles were varied for different cases. Table 1

summarizes the hydrodynamic properties of the dispersed phases for different cases studied.

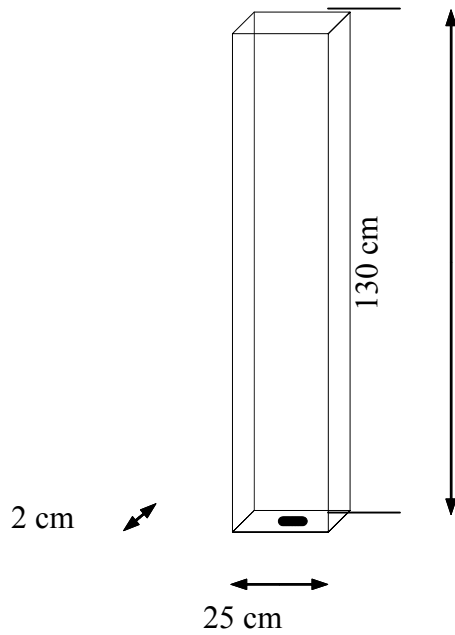


Figure 2. Schematics of the pseudo-two-dimensional bubble column.

Table 1. Hydrodynamic parameters for different cases

Case number	Bubble diameter mm	Superficial gas velocity mm/s	Bubble density kg/m <sup>3</sup>	Particle diameter mm	Particle density kg/m <sup>3</sup>	Particle loading
1	2.0	2.0	1.29	0.25	1000	0.3%
2	2.0	2.0	1.29	-	-	0.0%
3	1.5	0.844	1.29	0.25	1000	0.3%

No-slip boundary conditions were imposed on three walls of the column for the liquid phase and an outflow condition was assumed at the upper boundary of the column. Bubble-wall and particle-wall collisions were included in the model using a hard sphere collision model revised from the model developed by Hoomans et al. (1996) as described by equations (1-15)-(1-21), with  $m_a$  equals to infinite. The rotation of bubbles and particles, as well as, wall roughness effects was neglected. A restitution coefficient of 0.5 was used for both bubble-wall collision and particle-wall collision,

while friction coefficients of 0.02 and 0.1 were assumed for bubble-wall collision and particle-wall collision, respectively.

### 1.3.8 Free Surface Boundary Conditions

Proper modeling of liquid-gas free surface is important for accurate analysis of bubbly flows. The marker-and-cell (MAC) method (Harlow and Welch, 1965) was used to simulate the column free surface. The details of the MAC method were described by Griebel et al. (1998). They developed a time dependent computational model for analyzing two-dimensional single phase flow with free surface.

Neglecting the surface tension, density and viscosity of air, the boundary conditions on the free surface is given as (Landau, 1959; Berger and Gastiaux, 1988):

$$(\boldsymbol{\tau}_f + p\mathbf{I}) \cdot \mathbf{n} = 0 \quad (\text{on the free surface}) \quad (1-25)$$

where  $\boldsymbol{\tau}_f$  is the viscous stress tensor in liquid given by Equation (1-3) and  $\mathbf{n} = (n_x \mathbf{i} + n_y \mathbf{j})$  is the unit normal to the free surface. ( $\mathbf{i}$  and  $\mathbf{j}$  are unit vectors in x and y directions.) For two-dimensional flows, the components of (1-25) in normal and tangential direction are given by

$$-p + 2\mu \left( n_x n_x \frac{\partial u}{\partial x} + n_x n_y \left( \frac{\partial u}{\partial y} + \frac{\partial v}{\partial x} \right) + n_y n_y \frac{\partial v}{\partial y} \right) = 0 \quad (1-26)$$

$$2n_x m_x \frac{\partial u}{\partial x} + (n_x m_y + n_y m_x) \left( \frac{\partial u}{\partial y} + \frac{\partial v}{\partial x} \right) + 2n_y m_y \frac{\partial v}{\partial y} = 0 \quad (1-27)$$

where  $\mathbf{m} = (m_x \mathbf{i} + m_y \mathbf{j})$  is the unit vector tangent to the free surface.

### 1.3.9 Modeling Bubble-Free Surface Interaction

For a rising bubble approaching the free surface, Doublez (1991) reported that for  $We < 0.28$ , the bubble breaks free into the free surface, while the bubble bounces for impacts at higher Weber numbers. Based on the work of Doublez (1991), a simple model for interaction of bubbles with the free surface is used in this study. It is assumed that the bubbles that impact the column free surface

with Weber number less than 0.28 will break free and leave the column, while bubbles impacting at higher Weber numbers will bounce using a hard sphere model. A Restitution coefficient of 0.2 was used for bubble-free surface collisions for  $We > 0.28$ .

### 1.3.10 Numerical Procedure

The governing equations of the model were discretized using finite difference method in a structured equidistant staggered grid. The central and upwind (donor cell) discretization scheme was used for convective parts and an explicit time step was used for time updating. The results was implemented in a new computer code ELM3PF (Eulerian-Lagrangian Method for Three Phase Flow) for analysis of three phase flows. The new code was written in C, and was based on NaSt2D code, which was a code for single-phase flows with free surface developed by Griebel et al. (1998). The new code (ELM3PF) has the capability of simulating unsteady, two dimensional three-phase liquid-gas-solid flows with free surface.

In ELM3PF, the pressure Poisson equations for liquid phase are solved using successive over-relaxation (SOR) method. A fixed time step,  $\Delta t$ , which typically is 0.001s is used for liquid phase calculation. The code calculates the liquid phase velocity field first. When the new liquid velocity field is obtained, the code evaluates, the minimum time for next collision,  $dt$ . Here,  $dt$  is the minimum time of all possible collisions including bubble-bubble collisions, particle-particle collisions, particle-bubble collisions, bubble-wall collisions and particle-wall collisions. If  $dt$  is smaller than  $\Delta t$ , the code computes bubble and particle velocities and positions over the time duration  $dt$ . The next collision process is then analyzed, and the corresponding discrete phase velocities after the collision are evaluated. The code then computes the next minimum time for collision and repeats this procedure until the accumulation of these  $dt$ 's equals  $\Delta t$ . Thereafter the forces acting on the bubbles and particles are evaluated and transferred into the momentum equation for the liquid phase. The code then computes the new liquid velocity field. For a case that the minimum collision time  $dt$  is larger than  $\Delta t$ , the code compute the forces acting on the bubbles and particles, and transfer these forces into momentum equations for liquid phase and evaluates the new liquid velocity. Typically, 9940 bubbles and 1000 particles are used in this study. CPU time requirement depends on the number of particles, bubbles and grid cells. For a typical number of bubbles and particles for a computational grid of 1500 cells, evaluation of one second transient behavior of the liquid-gas-solid three-phase flow requires about 4 hours CPU time on a SUN Ultra10 workstation.

### 1.3.11 Effect of Grid Size

In order to check the sensitivity of the simulation result on the grid size, the grid spacing was reduced by a factor of two from 1cm to 0.5cm. Comparison of the two cases showed that the reduction of the grid size did not generate a noticeable difference in simulation results. Therefore, a grid spacing of 1cm was typically used.

## 1.4 Results and Discussion

### 1.4.1 Comparison with Experimental Data

We compared our model predictions with the experimental data of Delnoij, Kuipers and Swaaij (1997a). Their experiments were performed in a pseudo-two-dimensional bubble column. They measured the oscillation frequency of the bubble plumes in columns with five different aspect ratios for gas-liquid flows and found that a clear transition of the flow pattern occurs when the aspect ratio changes from 1 to 3. In a bubble column with an aspect ratio of 2.2, they used neutrally buoyant particles as tracer particles to visualize the liquid field. Figure 3 compares the present model predictions of the flow structure with the experimental data of Delnoij, et al. (1997a). The hydrodynamic parameters used in the simulation, which are identical to those of the experimental study, are listed in Table 1 (case 1). In Figure 3, the small dots show the liquid phase stream traces, while the small circles and the large circles show, respectively, the positions of the particles and bubbles. The model predictions appear to be in good agreement with the experimental data of Delnoij, et al. (1997a). The model not only predicts the proper S-shape path of the bubble plume, but also predicts the movements of large vortices and the oscillatory behavior of the bubble plume.

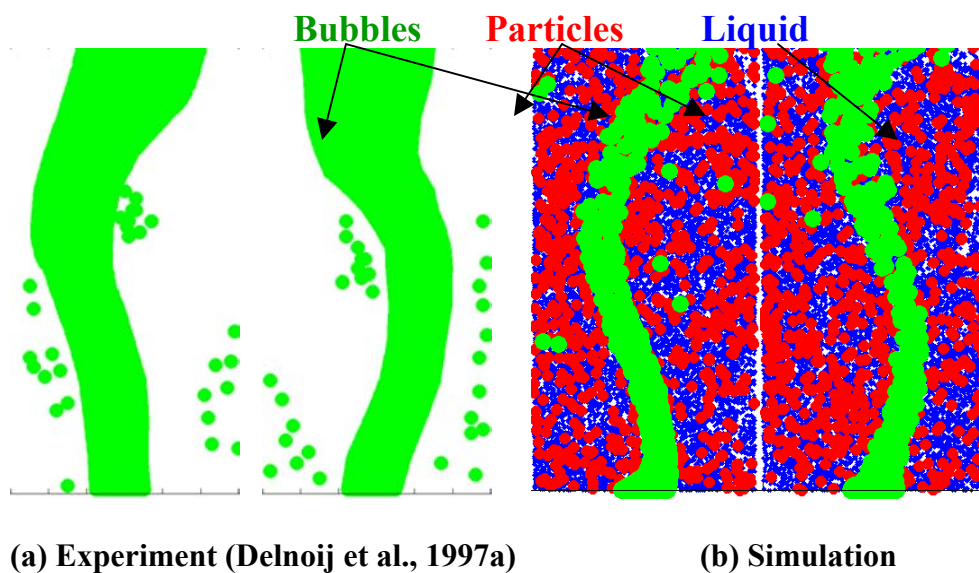


Figure 3. Flow structure in a three-phase bubble column with an aspect ratio of 2.2. Superficial gas velocity  $U_s = 2.0$  mm/s, bubble size  $d_b = 2.0$  mm.

Delnoij et al. (1997a) performed a series of experiments on bubble columns with different aspect ratios and evaluated the corresponding quasi-steady frequencies of the bubble plume oscillation. For conditions identical to the experiments, we performed a series of simulations for two-phase gas-liquid flows in the bubble column with different aspect ratios. Figure 4 compares the

model predictions for the oscillation frequency of the bubble plumes with the experimental data of Delnoij et al. (1997a). The simulation parameters are listed in Table 1 (case 2). This figure shows good agreement of the model predictions for the bubble plume oscillation frequencies with the experimental data. Delnoij et al. (1997a) also performed a computer simulation that predicted the S-shape path of the bubble plumes, but their model had difficulty in predicting the evolution of the large vortical motions and the oscillatory behavior of the bubble plume in the column. Their model neglected the presence of free surface and bubble-bubble coalescence. The presently developed model includes the liquid free surface and can predict the movement of the large vortex and the oscillatory behavior of the bubble plume in the column. This implies that the column free surface has important consequences and has to be accounted for in the computational model. It appears that the fluctuations of free surface affect the motion of both the fluid phase and dispersed phases in the column.

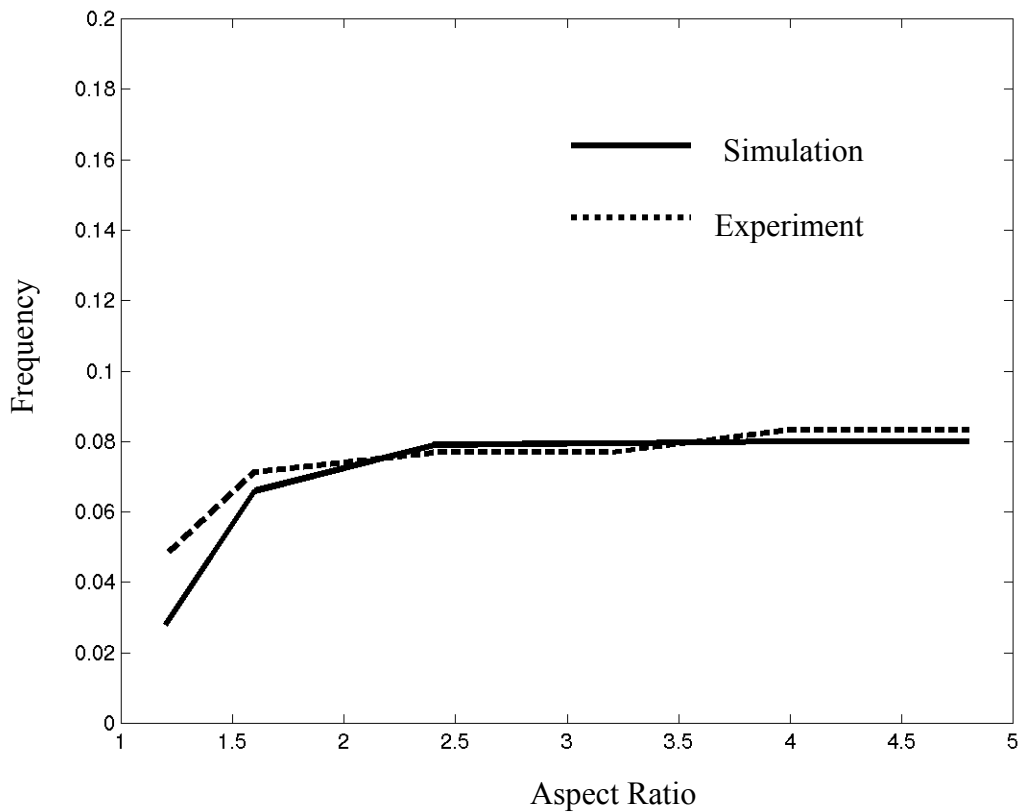


Figure 4. Comparison of the computed oscillation frequency of bubble plumes with the experimental data of Delnoij et al. (1997a). Superficial gas velocity  $U_s = 2.0$  mm/s, bubble size  $d_b = 2.0$  mm.

#### 1.4.2 Development of Transient Flow Structures

Figure 5 shows the snapshots of model predictions for the liquid stream traces, and the locations of bubbles and particles at times 1, 5, 9 and 13 seconds after initiation of the flow. The aspect ratio

of the column is 2.2 and the values of other parameters used in the simulation are listed in Table 1 (case 1). The evolution of the flow structure in the bubble column can be seen from this figure. Figures 6, 7 and 8, respectively, show the corresponding bubble velocities, liquid velocities and particle velocities at different times. The transient characteristics of the three-phase flow are clearly seen from these figures. In the first 4 seconds, bubble plume rises rectilinearly along the centerline of the column, which generates two vortices behind the plume head as seen in Figures 5a and 7a. These vortices are symmetric in the first second after initiation of the flow, but as the bubble plume approaches the column free surface, the vortices become non-symmetric. Figure 7 also shows that on the liquid velocities generated by the counter rotating vortices in the bottom of the vessel point to the center of the column, which tends to move the bubbles inside toward the centerline; thus, the bubble plume shrinks in this region. On the top, counter rotating vortices leads to liquid velocities pointing outward; this motion drags the bubbles toward the column walls. As a result, the head of the bubble plume expands, as seen more clearly in Figure 5.

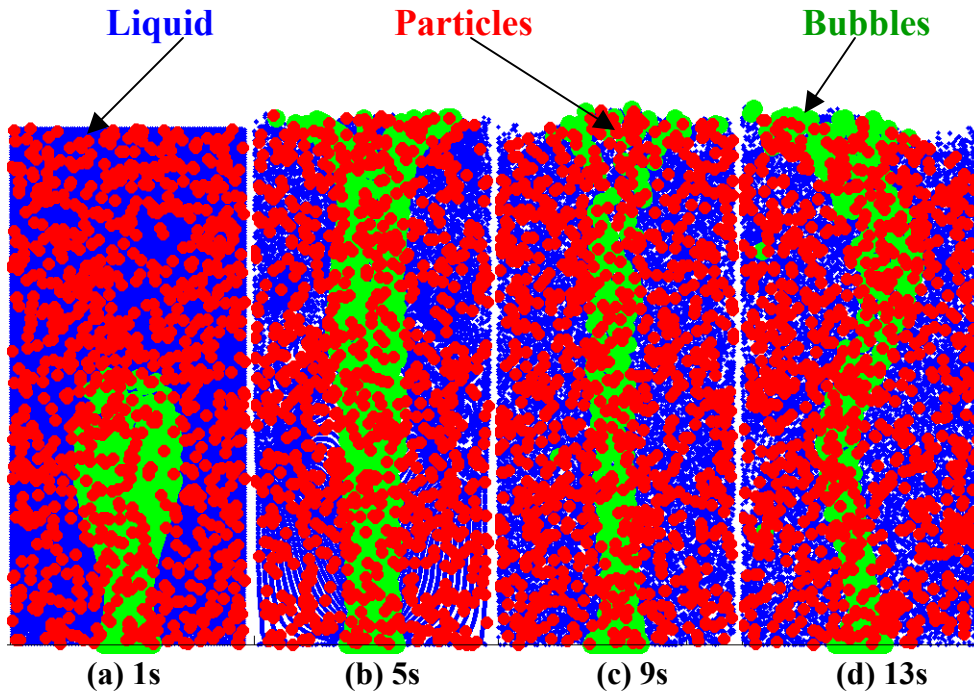


Figure 5. Computed flow structure of the gas-liquid-particle three-phase flow in a bubble column with an aspect ratio of 2.2. Superficial gas velocity  $U_s = 2.0$  mm/s, bubble size  $d_b = 2.0$  mm, particle size  $d_p = 0.25$  mm.

Figure 7d shows that when the bubble plume reaches the free surface of the column, staggered vortical flows in the column are formed. As a result, the bubble plume changes its path to S-shape that can be seen in Figure 5d. With the upward flow of the bubble plumes, these staggered vortices moves downward and result in an oscillation of the bubble plume as seen in Figure 5. Comparing Figures 5 and 7, shows that the evolution of the three-phase flow in the column is dominated by

these time-dependent staggered vortices.

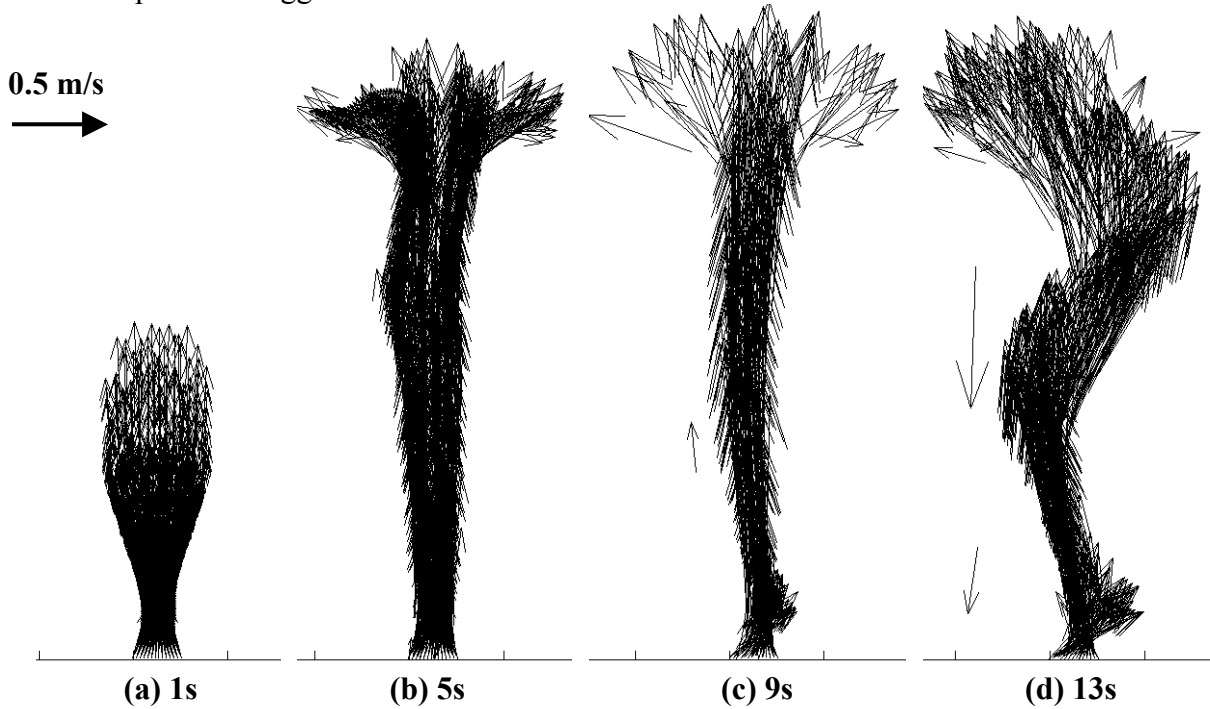


Figure 6. Computed snapshots of the bubble velocities of the gas-liquid-particle three-phase flow in a bubble column with an aspect ratio of 2.2. Superficial gas velocity  $U_s = 2.0$  mm/s, bubble size  $d_b = 2.0$ mm, Particle size  $d_p = 0.25$ mm.

Figures 5 and 7 show solid particles are concentrated mainly outside the large vortices in the regions with relatively high liquid velocities. This is, because of the centrifugal force that pushes the particles away from the center of the vortices. Some particles are retained inside these staggered vortices, partly because of particle-particle collisions that decrease particle segregation.

Comparison of Figures 5, 6 and 7 reveals another important feature of the three-phase flows in the column. It is seen that a number of bubbles are captured by the staggered vortices and move downward along with the vortices as shown in Figures 5d, 6d and 7d. In most cases, these captured bubbles are at some distance from the center of the vortices. Once those bubbles reach the bottom of the column, they turn upwards and move with the main bubble plume as seen in Figure 5c, 6c and 7c. Figures 5, 7 and 8, similarly show that particles are also captured by the vortices and are carried around by the time-dependent circulating motions. Comparing Figures 6, 7 and 8, also indicates that the bubble upward velocities are much larger than both particle and liquid, but bubble downward velocities are smaller than the other phases.

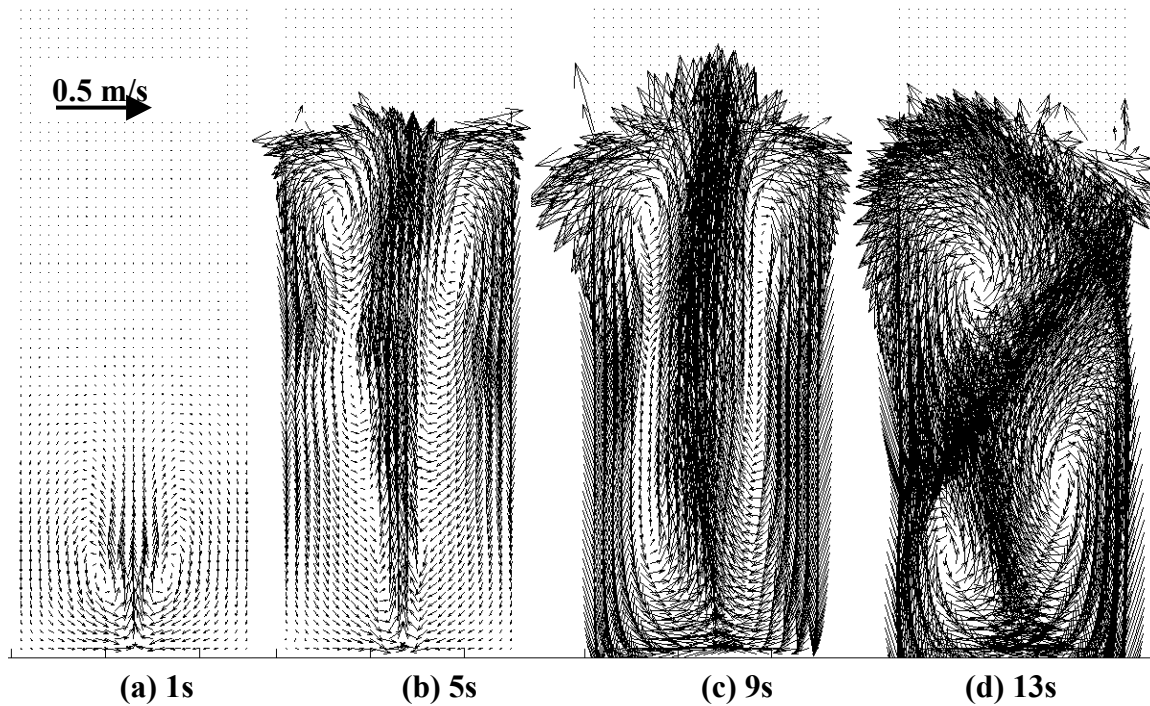


Figure 7. Computed snapshots of the liquid velocities of the gas-liquid-particle three-phase flow in a bubble column with an aspect ratio of 2.2. Superficial gas velocity  $U_s = 2.0$  mm/s, bubble size  $d_b = 2.0$ mm, particle size  $d_p = 0.25$ mm.

As for the magnitudes of particle and liquid velocities, they are of the same order, with particle downward and upward velocities being generally smaller than that of liquid. In some regions, particle upward velocities can be slightly larger than liquid velocities. The differences between the liquid and particle velocities are, generally, very small.

The reason for the observed velocity pattern can be explained by the effect of the buoyancy force of the bubbles, inertia of particles and viscosity of the liquid. The main driving force for the flow in the column is the rise of the bubbles due to the buoyancy effects. The bubbles then drag the liquid and the particles upwards along its time-evolving S-shape path. Thus, bubbles upward velocities in the column are naturally larger than both liquid and particle velocities.

In the regions outside the staggered vortices, where the liquid velocity is downward, the drag of liquid on the bubbles is also downward. The bubble buoyancy force, however, is upward, and thus the bubble can not follow the liquid closely. In this region the bubble velocities are smaller than both particle and liquid velocities.

The neutrally buoyant particles are generally being transported by the liquid, and thus the particle velocity is slightly smaller than the liquid. Occasionally particles with high velocities may entrain in low liquid velocity region. In these situations the particle local velocities may become

slightly larger than the liquid phase.

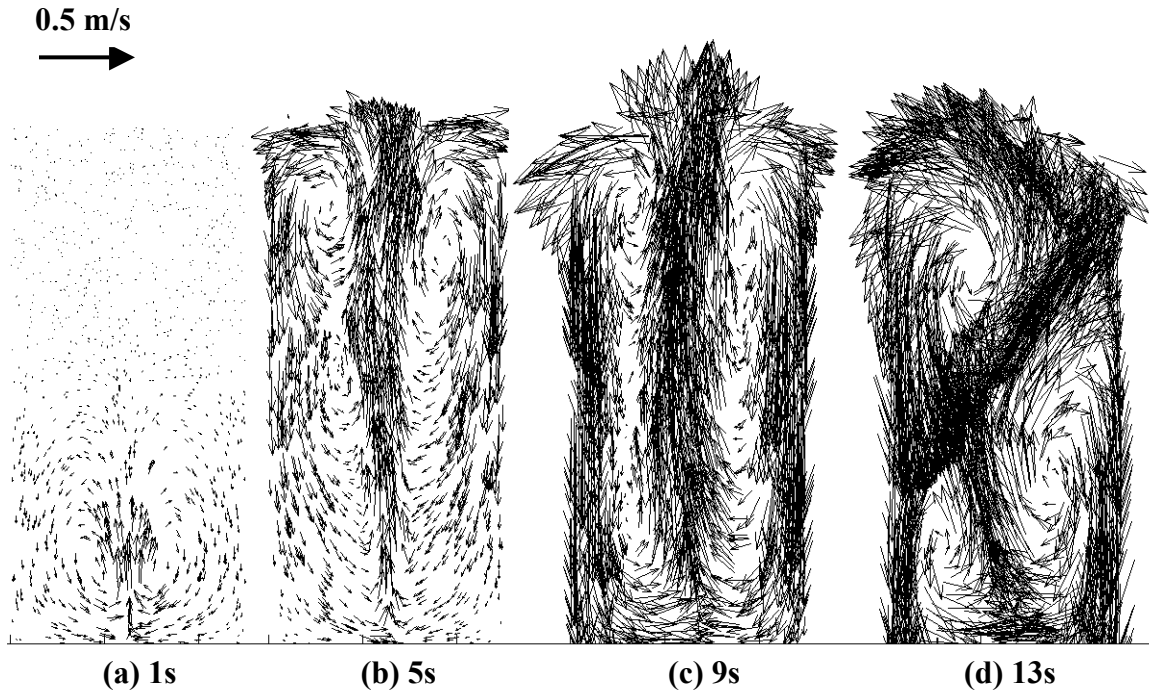


Figure 8. Computed snapshots of the particle velocities of the gas-liquid-particle three-phase flow in a bubble column with an aspect ratio of 2.2. Superficial gas velocity  $U_s = 2.0$  mm/s, bubble size  $d_b = 2.0$  mm, particle size  $d_p = 0.25$  mm.

Figure 9 shows the average velocities of the particles, bubbles and liquid at different sections across the bubble column. Here a space-time averaging method for time duration of 2 to 13 seconds was used. As expected, the bubble velocities are much larger than the particle and liquid velocities. The particle and the liquid velocities are of the same order. Along the center line of the column, all the three phase upward velocities increase with the height of the column, reaching their maximum values at the height of 0.4 m. The velocities then decrease with the height toward the free surface. Along the two side walls, the velocities are downward and the velocity magnitudes increase with the height of the column attaining their maximum values at about 0.45 m. Beyond this height, the velocities decrease toward the free surface. At the free surface the bubbles have positive net velocities as they leave the column. The horizontal component of the velocity shows that the liquid and the solid particles attain high outward velocities at the free surface. Figure 9 shows that the lower 2/3 height of the column, both upward velocities and downward velocities change slowly, while in the top 1/3 height of the column, the changes in velocity components are large. Figure 9 shows that the curves for the liquid and particle velocities are relatively smooth, while those for the bubbles are not. This is because of the statistical error to the relatively smaller number of samples for bubbles. The curves on the left side of Figure 9a indicate that a number of bubbles are captured by the downward moving vortices during the averaging time that the graph is generated.

While for the simulations shown in Figures 6-9 particles are neutrally buoyant, particle inertia due to their finite size affect their motion characteristics. In the lower part of the column, liquid upward velocities are accelerating; thus, the particle upward velocities are slightly smaller than the liquid velocities due to particle inertia. In the upper part of the column, liquid upward velocities are decelerating, and thus the particle upward velocities are slightly larger than the liquid velocities. For the downward velocities, the trend is just opposite.

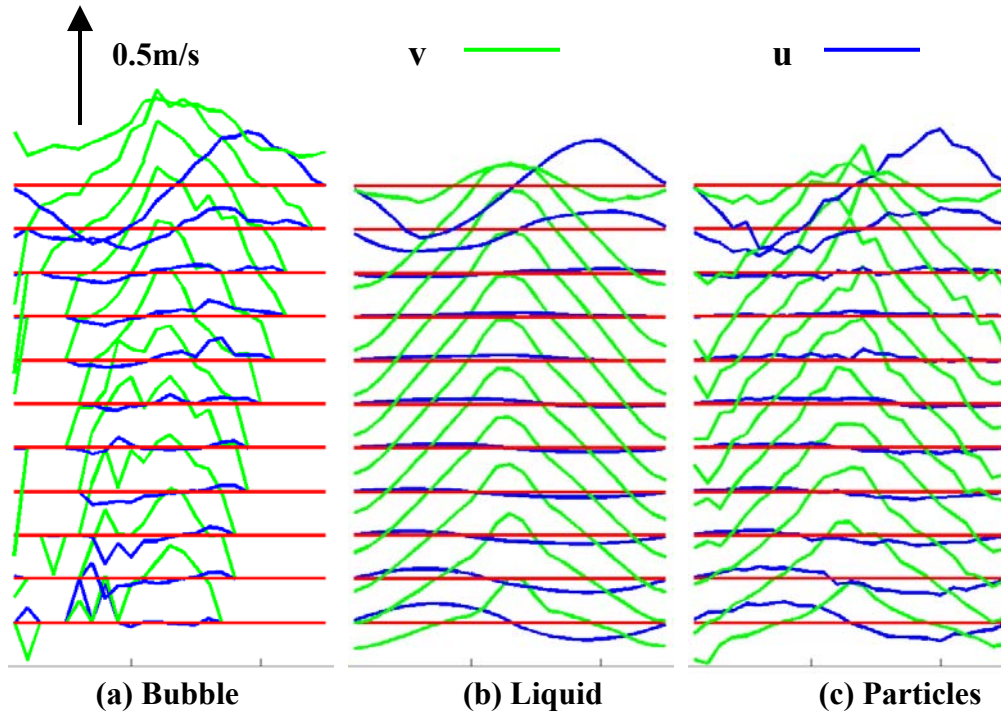


Figure 9. Average velocity profile of the bubbles, liquid and particles of the gas-liquid-particle three-phase flow in a bubble column with an aspect ratio of 2.2. Superficial gas velocity  $U_s = 2.0$  mm/s, bubble size  $d_b = 2.0$  mm, particle size  $d_p = 0.25$  mm.

## 1.5. Conclusions

In this study, an Eulerian-Lagrangian computational model for simulations of gas-liquid-solid flows in three-phase slurry reactors is presented. The two-way interactions between bubble-liquid and particle-liquid are included in the analysis. Particle-particle interactions and bubble-bubble interactions are accounted for by the hard sphere model approaches, and the bubble coalescence is also included in the model. The transient characteristics of three-phase flows are studied and the effects of bubble size on variation of flow patterns are discussed. On the basis of the presented results, the following conclusions are drawn:

- The transient characteristics of the three-phase flow in the bubble column are dominated by time-dependent staggered vortices, which are generated near the free surface and move downwards.
- The bubble plumes move along S-shape paths and exhibit an oscillatory behavior.
- Highest particle concentrations occur in the region outside the staggered vortices, in the regions with high liquid velocities.
- Most bubbles in the column form a main bubble plume, and only some bubbles are captured by the staggered vortices.
- Bubble upward velocities are much larger than both particle and liquid velocities. The bubble downward velocities are, however, smaller than both particle and liquid velocities.
- Bubble size has major effect on the characteristics of the three-phase flow. For the same number of bubbles, larger bubbles significantly increase the development of the flow characteristics. Compared to a column with small bubble, the column with large bubble has higher bubble, particle and liquid velocities and higher bubble plume oscillation frequency.
- Bubble velocities determine liquid velocities, and liquid velocities can affect bubble plume shape depending on the size of the bubbles.

## 2. TWO-PHASE FLOWS IN A DUCT WITH HEAT TRANSFER

The problem of two-phase flows with heat transfer in a duct is studied. The formulation of two-phase flows in a duct is presented in this section. The model accounts for the two-way interactions both in moment and energy transport.

### 2.1 Hydrodynamic Formulation

The equations of motion of turbulent flow field are obtained by applying the Reynolds decomposition on the instantaneous momentum equation. The closed time-dependent equation for the mean gas velocity in a vertical fully developed axisymmetric gas-solid flow in cylindrical coordinates is given as

$$\frac{D[(1-\phi)U_g]}{Dt} = \frac{1}{r} \frac{\partial}{\partial r} \left[ r(\nu + \nu_t)(1-\phi) \frac{\partial U_g}{\partial r} \right] - (1-\phi)g_o - \frac{(1-\phi)}{\rho_g} \frac{\partial p}{\partial x} + S_u \quad (2-1)$$

Here  $\phi$  is the solid volume fraction,  $S_u$  is the coupling source term due the interaction of gas and solid, and  $\nu_t = c_\mu f_\mu k \tau$ , is the eddy viscosity, where  $c_\mu = 0.09$ , and  $f_\mu$  is the damping function. In Equation (2-1),  $S_u$ , the coupling source term due to the presence of particle which is given as

$$S_u = \frac{\rho_p}{\tau_p \rho_g} \left[ \phi_p (U_p - U_g) \right] \quad (2-2)$$

where  $\tau_p$  is the particle dynamic relaxation time, defined as

$$\tau_p = \frac{4}{3} \frac{\rho_p d_p}{\rho_g C_D |U_p - U_g|} \quad (2-3)$$

and  $C_D$  is the Drag coefficient.

For an axisymmetric fully developed two-phase flow, the resulting  $k-\tau$  transport equations are given as

$$\frac{D(1-\phi)k}{Dt} = \frac{1}{r} \frac{\partial}{\partial r} \left[ r(1-\phi) \left( \nu + \frac{\nu_t}{\sigma_k} \right) \frac{\partial k}{\partial r} \right] + \nu_t (1-\phi) \left( \frac{\partial U_g}{\partial r} \right)^2 - (1-\phi)\varepsilon - S_k \quad (2-4)$$

$$\begin{aligned} \frac{D(1-\phi)\tau}{Dt} = & \frac{1}{r} \frac{\partial}{\partial r} \left[ r(1-\phi) \left( \nu + \frac{\nu_t}{\sigma_\tau} \right) \frac{\partial \tau}{\partial r} \right] + c_{\tau 1} (1-\phi) - c_{\tau 2} (1-\phi) \frac{\tau}{k} \nu_t \left( \frac{\partial U_g}{\partial r} \right)^2 \\ & + \frac{2}{k} (1-\phi) \left[ \left( \nu + \frac{\nu_t}{\sigma_\tau} \right) \frac{\partial \tau}{\partial r} \frac{\partial k}{\partial r} \right] - \frac{2}{\tau} (1-\phi) \left[ \left( \nu + \frac{\nu_t}{\sigma_\tau} \right) \frac{\partial \tau}{\partial r} \frac{\partial \tau}{\partial r} \right] + S_\tau \end{aligned} \quad (2-5)$$

The coefficients in Equations (2-4) and (2-5) are given as  $c_{\tau 1} = 0.92$ ,  $c_{\tau 2} = 0.44$ ,  $\sigma_k = 1$ , and  $\sigma_\tau = 1$ . In Equation (2-4),  $S_k$  is the source term due to the solid phase interaction with gas. i.e.,

$$S_k = -\frac{\rho_p}{2\rho_g \tau_p} \left[ \overline{\phi(u_i^{p'} u_i^{g'} - u_i^{g'} u_i^{g'})} + \overline{\phi' u_i^{g'} (U_p - U_g)} \right] - \frac{\rho_p}{2\rho_g \tau_p} \left[ \overline{\phi' u_i^{g'} (u_i^{p'} - u_i^{g'})} \right] \quad (2-6)$$

Here  $u_i^{g'}$  and  $u_i^{p'}$  are, respectively, the fluctuation velocities of gas and particle phases, and  $\phi'$  is the particle concentration fluctuation. Neglecting the triple correlation terms, the coupling term becomes

$$S_k = -\frac{\rho_p}{2\rho_g \tau_p} \left[ \overline{\phi(u_i^{p'} u_i^{g'} - u_i^{g'} u_i^{g'})} + \overline{\phi' u_i^{g'} (U_p - U_g)} \right] \quad (2-7)$$

The source term in the Equation (2-5) is given as

$$S_\tau = \frac{S_k}{\varepsilon} (c_{\tau 3} - 1) \quad (2-8)$$

Here, coefficient  $c_{\tau 3} = 2.0$  is used.

The gas-particle velocity correlation term  $\overline{u_i^{p'} u_i^{g'}}$  in Equation (2-7) is evaluated using a combined Eulerian-Lagrangian averaging procedure. First the mean particle velocity,  $U_p = U_1^p$ , during each

Lagrangian time step is evaluated within a computational control volume (computational cell) around each node by ensemble averaging. Then the cross correlation term  $\overline{u_i^p u_i^g}$  is evaluated by the following averaging procedure:

$$\overline{u_i^p u_i^g} = \frac{1}{\Delta t_E N_p} \sum_{k=1}^{N_t} \sum_{n=1}^{N_p} [(u_i^p - U_i^p)(u_i^g - U_i^g)] \Delta t_L \quad (2-9)$$

where  $u_i^p$  is the instantaneous particle velocity, and  $u_i^g$  is the instantaneous gas velocity. Here,  $N_p$  is the number of particle in the computational cell,  $\Delta t_E = N_t \cdot \Delta t_L$  and  $N_t$  is the number of Lagrangian time steps in each Eulerian time step. In Equation (2-9), the summation over n (and division by  $N_p$ ) indicates the ensemble averaging over the particles in each computational cell, and the summation over k (and division by  $N_t$ ) denotes the temporal averaging over the Eulerian time step.

The particle concentration- gas velocity correlation term is modeled using a gradient transport hypothesis. That is,  $\overline{\phi' u_i^g} \approx \frac{v_i}{\sigma_{pg}} \frac{\partial \phi}{\partial r}$ , where,  $\sigma_{pg}$  is taken to be a constant equal to 1.

## 2.2 Thermal Formulation

The equation governing the mean turbulent gas temperature is given as

$$\frac{D(1-\phi)T}{Dt} = \frac{1}{r} \frac{\partial}{\partial r} \left[ r(1-\phi)(\alpha + \alpha_t) \frac{\partial T}{\partial r} \right] + S_T \quad (2-10)$$

The thermal eddy diffusivity is by  $\alpha_t = c_\lambda f_\lambda k \tau_\theta$ . Here  $\tau_\theta$  represents thermal time scale,  $c_\lambda$  is a constant, which is assumed to be equal to 0.2, and  $f_\lambda$  is a damping function. The second term on the right hand side of Equation (2-10) is the coupling term due to the solid phase interaction with the gas. i.e.,

$$S_T = \frac{F}{\rho_g c_{pg}} [\phi (T_p - T_g)] \quad (2-11)$$

where  $F = 6Nu_p K_g / d_p^2$ .

The resulting  $k_\theta - \tau_\theta$  transport equations for an axisymmetric fully developed two-phase flow are given as

$$\frac{D(1-\phi)k_\theta}{Dt} = \frac{1}{r} \frac{\partial}{\partial r} \left[ r(1-\phi) \left( \alpha + \frac{\alpha_t}{\sigma_{k\theta}} \right) \frac{\partial k_\theta}{\partial r} \right] + \alpha_t \left( \frac{\partial T_g}{\partial r} \right)^2 - \varepsilon_\theta - S_{k\theta} \quad (2-12)$$

$$\begin{aligned}
\frac{D(1-\phi)\tau_\theta}{Dt} = & \frac{1}{r} \frac{\partial}{\partial r} \left[ r(1-\phi) \left( \alpha + \frac{\alpha_t}{\sigma_{\tau\theta}} \right) \frac{\partial \tau_\theta}{\partial r} \right] + c_{\tau\theta 1} (1-\phi) \frac{\tau_\theta}{k_\theta} \alpha_t \left( \frac{\partial T_g}{\partial r} \right)^2 + c_{\tau\theta 2} (1-\phi) \frac{\tau_\theta}{k} v_t \left( \frac{\partial U_g}{\partial r} \right)^2 \\
& + (c_{\tau\theta 3} - 1)(1-\phi) + \frac{2}{k_\theta} (1-\phi) \left[ \left( \alpha + \frac{\alpha_t}{\sigma_{\tau\theta}} \right) \frac{\partial \tau_\theta}{\partial r} \frac{\partial k_\theta}{\partial r} \right] - \frac{2}{\tau_\theta} (1-\phi) \left[ \left( \alpha + \frac{\alpha_t}{\sigma_{\tau\theta}} \right) \frac{\partial \tau_\theta}{\partial r} \frac{\partial \tau_\theta}{\partial r} \right] \\
& + c_{\tau\theta 4} (1-\phi) \frac{\tau_\theta}{\tau} + S_{\tau\theta}
\end{aligned} \tag{2-13}$$

The model coefficients in Equations (2-12) and (2-13) are

$$c_{\tau\theta 1} = 0.27, \quad c_{\tau\theta 2} = -0.7, \quad c_{\tau\theta 3} = [1 - \exp(-y^+ / 4.8)]^2, \quad c_{\tau\theta 4} = (1.92 - 1)[1 - \exp(-y^+ / 4.9)]^2$$

In Equation (2-12),  $S_{k\theta}$ , is the source term due to the solid phase interaction with gas, and is given by

$$S_{k\theta} = -\frac{F}{2\rho_g c_{pg}} \left[ \overline{\phi' (t'_p t'_g - t'_g t'_g)} + \overline{\phi' t'_g (T_p - T_g)} \right] \tag{2-14}$$

where  $t'_g$  is the fluctuating gas temperature and  $t'_p$  is the fluctuating particle temperature. The correlation terms between particle concentration and gas temperature are modeled by a gradient transport hypothesis given as  $\overline{\phi' t'_g} \approx \frac{\alpha_t}{\sigma_{tg}} \frac{\partial \overline{\phi}}{\partial r}$ , where,  $\sigma_{tg} = 1$  is a constant.

The gas-particle temperature correlation term  $\overline{t'_p t'_g}$  in Equation (2-14) is evaluated using a combined Eulerian-Lagrangian averaging procedure similar to that used for the gas-particle velocity correlation. First the mean particle temperature,  $T_p$ , during each Lagrangian time step is evaluated within a computational control volume (computational cell) around each node by ensemble averaging. Then the cross correlation  $\overline{t'_p t'_g}$  is evaluated by ensemble averaging over the particles in each computational cell and temporal averaging over the Eulerian time step similar to the procedure described for the velocity cross correlation.

### 2.3 Instantaneous Turbulence Fluctuation

The generation of fluctuating components of fluid velocity using a continuous Gaussian random field model was suggested by Kraichnan. Accordingly, the fluctuation component of the turbulence in an isotropic field is given by

$$\bar{u}^+(\bar{X}^+, t^+) = \sqrt{\frac{2}{M}} \left\{ \sum_n^M \bar{U}_1 [\cos(\bar{K}_n \cdot \bar{X}^+ + \omega_n t^+)] \right\} + \sqrt{\frac{2}{M}} \left\{ \sum_n^M \bar{U}_2 [\sin(\bar{K}_n \cdot \bar{X}^+ + \omega_n t^+)] \right\} \quad (2-15)$$

where  $\bar{X}^+$  is the position vector and all quantities are nondimensionalized with a velocity scale  $u^*$  and kinematic viscosity. That is

$$u_i^+ = \frac{u_i}{u^*}, t^+ = \frac{tu^{*2}}{\nu}, x_i^+ = \frac{x_i u^*}{\nu} \quad (2-16)$$

In Equation (2-15)

$$\bar{U}_1 = \bar{\zeta}_n \times \bar{K}_n, \quad \bar{U}_2 = \bar{\xi}_n \times \bar{K}_n, \quad \bar{K}_n \cdot \bar{U}_1 = \bar{K}_n \cdot \bar{U}_2 = 0. \quad (2-17)$$

The components of vectors  $\bar{\zeta}_n$ ,  $\bar{\xi}_n$ , and frequencies  $\omega_n$  are picked independently from a Gaussian distribution with a standard deviation of unity. Each component of  $\bar{K}_n$  is also a Gaussian random number with a standard deviation of  $1/2$ . In Equation (2-15) M is the number of terms in the series. (Here M = 100 is used.)

Equation (2-15) generates a continuous incompressible Gaussian random field, which resembles an isotropic homogeneous turbulence. For application to nonhomogeneous flows a scaling is needed. Here a similar scaling is used using the available data for turbulent velocity field.

The approach is also extended and used for generating the temperature fluctuations. That is, the nondimensional fluctuation temperature is evaluated from

$$t^+(\bar{X}^+, t^+) = \sqrt{\frac{2}{M}} \left\{ \sum_n^M T_1 [\cos(\bar{K}_n \cdot \bar{X}^+ + \omega_n t^+)] \right\} + \sqrt{\frac{2}{M}} \left\{ \sum_n^M T_2 [\sin(\bar{K}_n \cdot \bar{X}^+ + \omega_n t^+)] \right\} \quad (2-18)$$

Here  $t^+ = t'_g / t^*$  with  $t^*$  being the root-mean square gas temperature fluctuation. All random coefficients in Equation (2-18) are generated similar to that of the Kraichnan model for the flow field, except for  $T_1$  and  $T_2$  that are picked from independent Gaussian distributions with a standard deviation of unity.

## 2.4 Particle Lagrangian Simulation

A Lagrangian particle tracking approach is used in the analysis. The equation of motion for a spherical particle including the viscous drag and gravitational forces is given by

$$\frac{du_i^p}{dt} = \frac{3C_d \rho_g}{4d_p \rho_p} |u_i^g - u_i^p| (u_i^g - u_i^p) + g \quad (2-19)$$

$$\frac{dx_i^p}{dt} = u_i^p \quad (2-20)$$

Here  $u_i^p$  is the particle velocity,  $u_i^g$  is the instantaneous fluid velocity with  $u_i^g = U_i^g + u_i^{g'}$ , where  $U_i^g$  is the fluid mean velocity and  $u_i^{g'}$  is the fluctuating component. In Equation (2-19)  $C_d$  is the local drag coefficient, which is a function of particle Reynolds number.

When a particle strikes a wall, it is assumed that it will bounce from the surface. The rebound velocity of a solid particle from the wall is evaluated using the classical impulse equation for inelastic collisions. Here unless stated otherwise a coefficient of restitution of 0.7 is used.

Thermal energy equation of the particles is given as

$$m c_p \frac{dT^p}{dt} = h_p A (T^g - T^p) \quad (2-21)$$

where  $m$  is the particle mass,  $c_p$  is the particle heat capacity,  $A$  is the particle surface area and  $h_p$  is the heat transfer coefficient. The term on the right hand side of (2-21) is due to the gas-particle heat transfer. Here  $T^p$  is the particle temperature, and  $T^g$  is the fluid temperature at the particle location.

Note that  $T^g = T_i^g + t^{g'}$ , where  $t^{g'}$  is the gas fluctuating temperature, which is generated using the extended Kraichnan model given by Equation (2-18). The convection transfer coefficient  $h_p$  is given as

$$Nu_p = \frac{h_p d}{k_g} = 2 + 0.6 Re_p^{0.5} Pr^{0.3} \quad (2-22)$$

$Nu_p$  is the Nusselt number,  $k_g$  is the gas heat conductivity, and  $Pr$  is the Prandtl number.

It should be emphasized that the mean gas velocity and temperature are evaluated from the Eulerian field equations. The instantaneous gas velocity and temperature at the particle location are then determined by adding the fluctuation fields as given by Equations (2-15) and (2-18) to the mean fields. The instantaneous values are then used in Equations (2-19) and (2-21) for evaluating the particle motion and temperature.

## 2.5 Results and Comparison with Experimental Data

Experimental data of Tsuji et al. (1984) were used to validate the hydrodynamic part of computational model. The experimental data of Tsuji et al. (1984) for a mass loading ratio (solid

mass flux/gas mass flux) of 1.13, and gas Reynolds number of 32000 in a vertical pipe of 30.5-mm inner diameter are reproduced in Figure 10. In the experiment the gas centerline velocity was 18.9 m/s and the particles were polystyrene spheres with a density of  $1020 \text{ kg/m}^3$  and a diameter of  $200 \mu\text{m}$ . Using the Eulerian-Lagrangian computational model, the gas particle flows for the condition of Tsuji et al. (1984) is simulated and results are plotted in Figure 10. Figure 10 shows that the predicted mean gas and particle velocities are in good agreement with the experimental data.

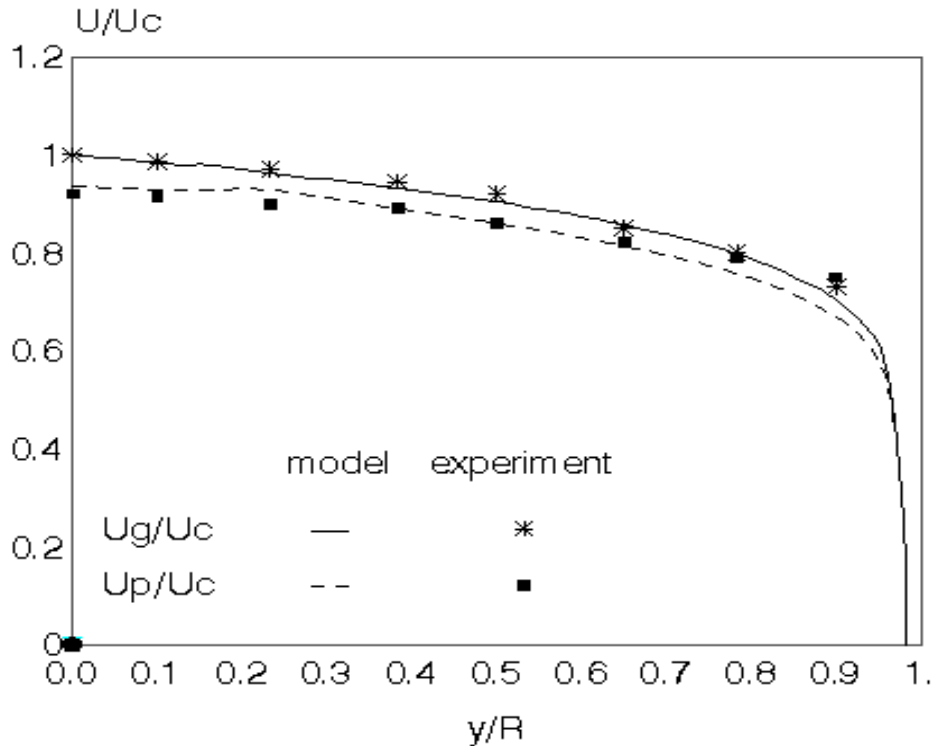


Figure 10. Gas and particle velocity profiles at mass loading ratio of  $Z=1.13$ . Comparison with The experimental data of Tsuji et al. 1984) for  $d_p = 200 \mu\text{m}$  and  $\text{Re}=32000$ .

Figure 11 compares the simulated particulate turbulence intensity with the experimental data of Tsuji et al. (1984) for a mass loading ratio of 1.3. In this figure, the solid squares represent the experiment data. This figure shows that the model predictions for the particulate turbulence intensity are in good agreement with the experimental data.

In this section comparison of the numerical predictions with the experimental data of Depew and Farber (1963) are presented. Depew and Farber (1963) measured the variation of the

mean suspension heat transfer coefficient with the mass loading ratio,  $Z$ . Their experiment was performed for a vertical pipe flow with a diameter of 0.019 m, with a constant wall heat flux. The fluid medium was air containing glass spherical particles with a diameter of  $200 \mu\text{m}$  and a gas Reynolds number of 13500.

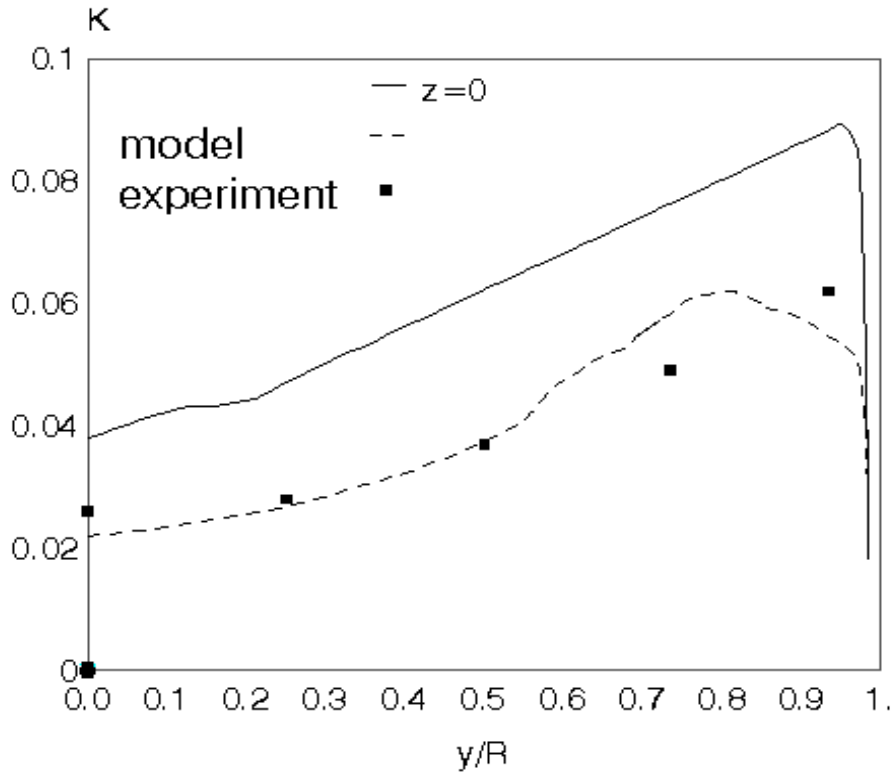


Figure 11. Comparison of gas turbulence intensity for mass loading ratio of  $Z=1.3$  with data of Tsuji et al. (1984) for  $d_p = 200 \mu\text{m}$  and  $Re=32000$ .

Figure 12 shows the comparison of the model predictions with the experimental data of Depew and Farber (1963) at a length/diameter ratio of  $x/D=46.4$ . At this length/diameter ratio, a fully developed condition may be assumed to prevailed in the pipe. Here, the suspension Nusselt number is given by

$$Nu = \frac{2Rq_w}{k_g(T_w - T_m)} \quad (2-23)$$

where  $T_m$ , is the mean suspension temperature, which is evaluated as

$$T_m = \frac{\int c_{pg} \rho_g (1-\phi) U_g T_g dA + \int c_{pp} \rho_p \phi U_p T_p dA}{\int c_{pg} \rho_g (1-\phi) U_g dA + \int c_{pp} \rho_p \phi U_p dA} \quad (2-24)$$

The thermal conductivity of gas is computed at the film temperature  $(T_m + T_w)/2$ . Heat transfer coefficient for single-phase gas flow is evaluated using a well established correlation,

$$Nu_o = 0,023 Re^{.8} Pr^{.4} . \quad (2-25)$$

Figure 12 shows good agreement between the model prediction for the heat transfer coefficient and the experimental data of Depew and Farber (1963).

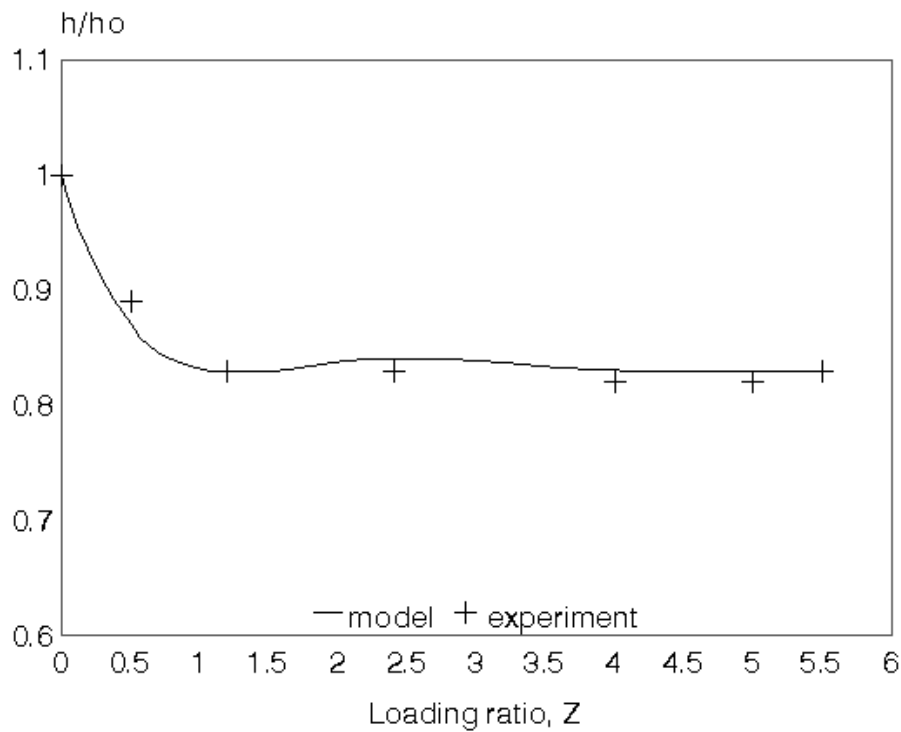


Figure 12. Predicted ratio of suspension heat transfer coefficient to gas heat transfer coefficient. Comparison with the experimental data of Depew and Farber (1963) for  $d_p = 200 \mu m$  and  $Re=13500$ .

## 2.6 Conclusions

A new model for analyzing heat transfer in turbulent two-phase gas-solid flows was developed. The model is based on two-way interaction of two-phase flows in an Eulerian/ Lagrangian formulation. The model includes the effect of thermal turbulence fluctuations and presents new

$k_\theta - \tau_\theta$  model equations, in addition to the  $k - \tau$  model for two-phase flows. Thus, the thermal eddy diffusivity is directly evaluated from the gas thermal turbulence intensity field. The coupling source terms in the thermal turbulent gas phase equations due to the presence of the solid phase is introduced. The source term in  $k_\theta$  equation is consisted of two main parts. One part is due to the difference between the mean temperatures of gas and solid phases, and the correlation between the particle concentration fluctuation and the temperature. The other term includes the correlation term between the gas and solid fluctuating temperatures. The model also directly evaluates the turbulence Prandtl number. The new model was used and computer simulations were performed and the mechanisms that control the behavior of suspension heat transfer coefficient especially near its minimum point was studied. Numerical model validation was performed for an upward pipe gas-solid flow with constant wall heat flux. On the basis of the results presented the following conclusions are drawn:

- The simulation results are in good agreement with the available experimental data.
- The heat transfer coefficient for two-phase flows varies with flow Reynolds number, mass loading and particle size
- The gas turbulence Prandtl number depends on mass loading ratio, flow Reynolds number and particle diameter.
- The model simulation results show that the solid phase causes thermal turbulence fluctuation to attenuate near the wall.
- For the range of Reynolds numbers and particle sizes studied, the heat transfer coefficient appears to have a minimum at a certain mass loading ratio. The minimum heat transfer coefficient appears to occur at the range of mass loading ratio for which the temperature fluctuation near wall also reaches to a minimum.

### 3. TWO-PHASE FLOWS IN HORIZONTAL AND INCLINED DUCTS

Using the earlier developed thermodynamically consistent model, a computational procedure for solving dense and dilute two-phase flows in ducts at various angles was developed. Figure 13 shows the configuration of the flow domain. The computational model predictions for mean flow and particle velocities, and phasic turbulence intensities were compared with the experimental data of Tsuji et al. (1989) for a horizontal duct flow. In addition, the variations of phasic shear and normal stresses, as well as the phasic fluctuation energy production and dissipation were also evaluated.

Using a Laser-Doppler Velocimeter (LDV), Tsuji et al. (1989) reported measurements of the phasic flow properties in a fully developed, two-phase turbulent flow in a horizontal channel with a height of 25 mm. In their experiments, polystyrene spheres with density of  $1038 \text{ kg/m}^3$  and an average diameter of 1.1 mm were used. A restitution coefficients of  $r = 0.93$  for particle-particle collisions, and a coefficient of dynamic friction  $\mu = 0.28$  between a particle and the wall were used in the present study. These values are identical to those reported by Tsuji et al. (1989).

The phasic mean velocities, turbulence intensities and solid volume fraction profiles for a mass loading of  $m = 1$  of 1.1-mm polystyrene spheres are shown in Figure 14. In this case, the channel mean velocity was  $= 7$  m/s. Figure 14a shows that the mean particulate velocity has a nearly uniform distribution and is generally smaller than the fluid mean velocity. The fluid velocity develops an asymmetric distribution with the peak velocity drifting to above the centerline. This is because the particle drag retardation of the fluid phase is larger near the lower wall due to higher concentration there. Figure 14a shows that the predicted fluid phase velocity is in good agreement with the experimental data while the particulate phase mean velocity is somewhat underestimated.

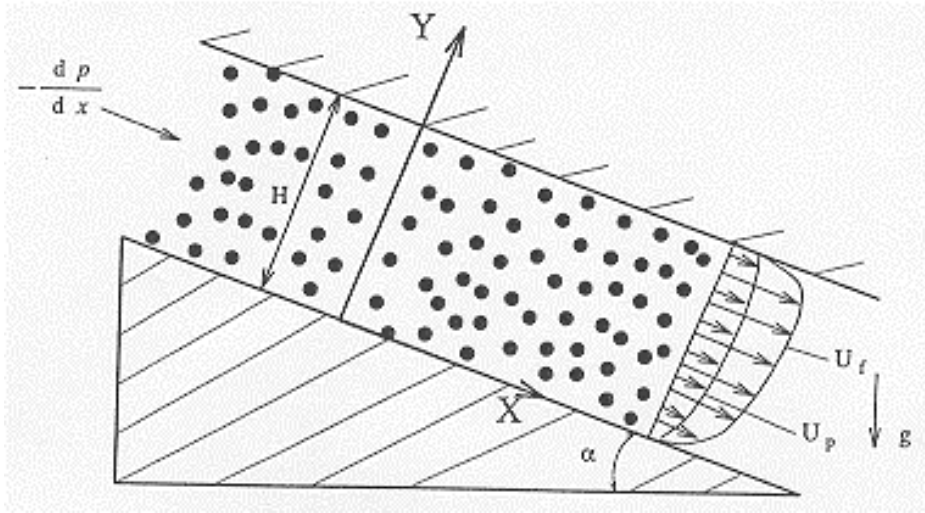


Figure 13. Configuration of the flow in duct an angle.

Figure 14b presents the predicted phasic fluctuation kinetic energy profiles. It is observed that the fluctuation kinetic energy for the fluid phase has peaks near both walls. The peak near the upper wall is larger than that near the lower wall. This implies that the presence of high concentration of particles reduces the fluid turbulence intensity. The particulate fluctuation kinetic energy profile is quite flat and smaller than that of the fluid phase, particularly near the walls. The solid volume fraction profile shown in Figure 14c clearly shows the strong segregation of particles toward the bottom wall. Clearly the gravity causes the heavier solid particles to migrate toward the lower wall of the horizontal channel. The experimental data for solid volume fraction, as reported by Tsuji et al. (1989), is reproduced in Figure 14c for comparison. It is observed that the agreement of the model predictions with the experimental data is quite good.

Figure 15 presents the model predictions for a gas-particle two-phase flow in a horizontal channel with a loading of  $m=3$ , an average solid fraction  $v_a = 0.0062$  and a comparison with the corresponding experimental data of Tsuji et al. (1989). The rest of the parameters used in this simulation are kept the same as those used in Figure 14. Figure 15a shows the variation of phasic mean velocity profiles. It is observed that the particulate phasic mean velocity is almost constant across the channel and is about one half of the fluid mean velocity. Fluid mean velocity has an

asymmetric profile with a peak in the upper part of the duct. Comparing Figures 14 and 15, it is observed that as loading,  $m$ , increases from 1 to 3, the particulate mean velocity remains nearly unchanged. The mean fluid velocity profile also has the same trend of variation, while the location of the peak mean velocity is drifted closer to the upper wall. As expected, the retardation effect of particle drag on the fluid phase increases with the increase of mass loading. Figure 15a also shows that the model predictions for the particulate mean velocity are in close agreement with the experimental data of Tsuji et al. (1989). Unfortunately, the experimental data for the fluid velocity was not reported for additional comparison.

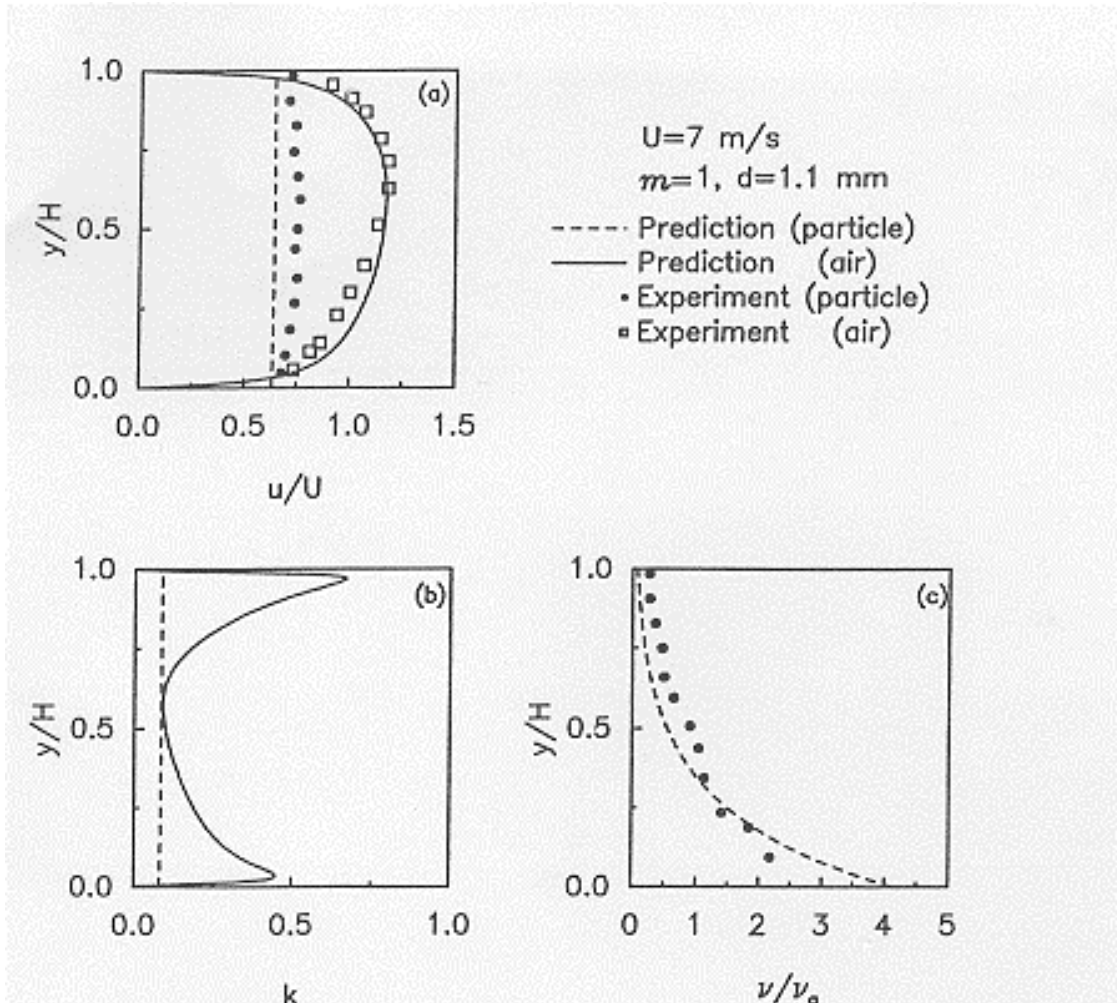


Figure 14. Variations of mean velocities, fluctuation kinetic energies and solid volume fraction profiles in a horizontal duct. Comparison with the data of Tsuji et al. (1989).

The corresponding phasic fluctuation kinetic energy profile for  $m=3$  ( $v_a = 0.08$ ) is shown in Figure 15b. It is observed that, while the particulate fluctuation kinetic energy is uniform and remained nearly unchanged, the fluid fluctuation kinetic energy has now a highly asymmetric distribution. Comparing Figure 15b to 14b, it is found that as the mass loading ratio increases, the fluid fluctuation kinetic energy near the bottom wall decreases, while that near the upper wall of the channel is not affected significantly. This is because the local concentration of the particles is quite low near the upper wall even at the higher loading of  $m=3$ . The solid volume fraction profile plotted in Figure 15c shows that the particle concentration is extremely high near the bottom wall. Figure 15c also shows that there is a reasonable agreement between the model prediction for the particle concentration and the experimental data of Tsuji et al (1989).

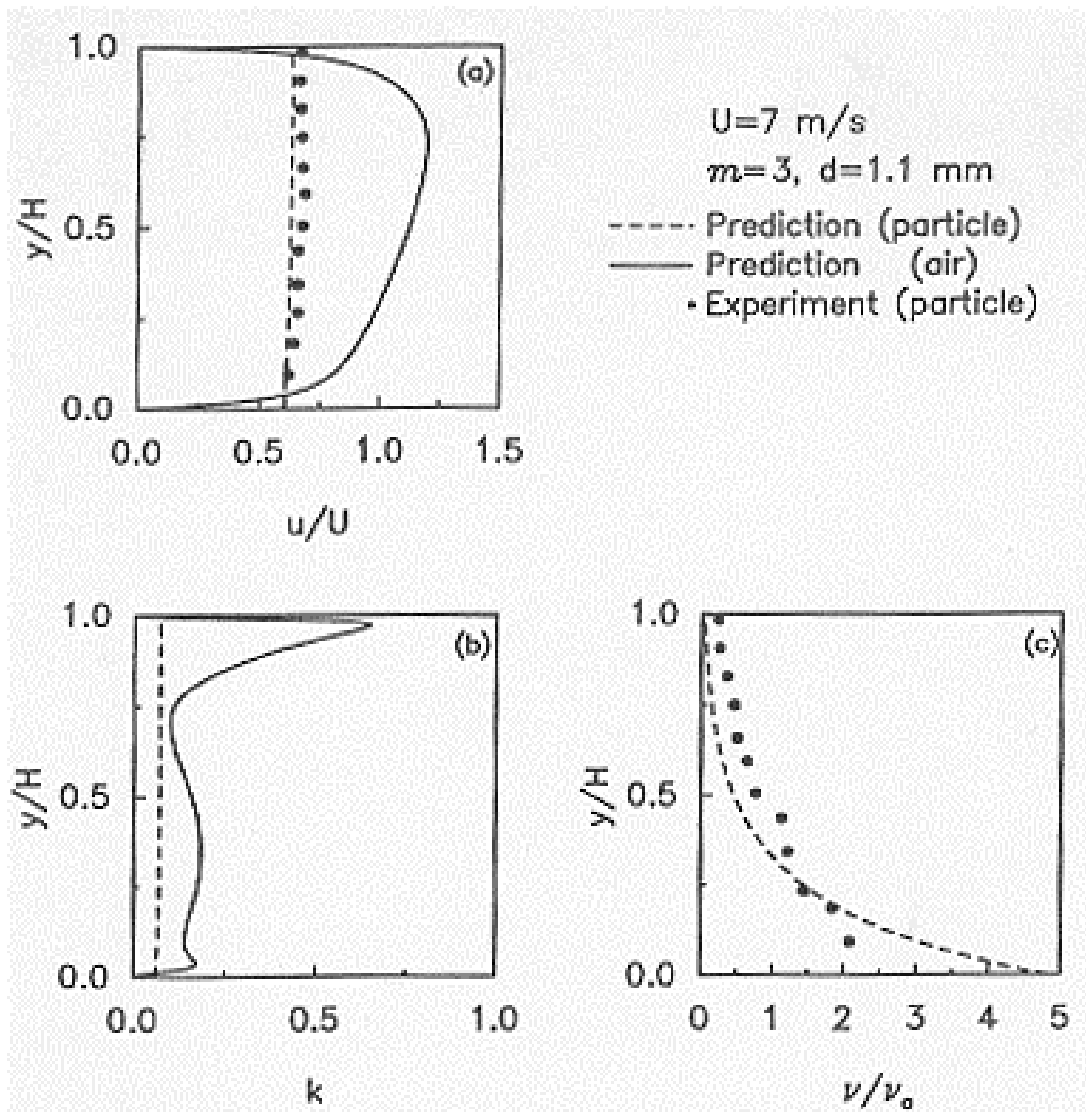


Figure 15. Variations of mean velocities, fluctuation kinetic energies and solid volume fraction profiles in a horizontal duct. Comparison with the data of Tsuji et al. (1989). For a gas-particle

mixture conveyed in a horizontal channel with a mass loading ratio of  $m=1$  ( $v_a = 0.0028$ ), and the mean average air velocity of  $U=15$  /s, the model predictions for solid volume fraction are shown in Figure 16. There is a large particle concentration near the lower wall and the solid volume fraction decreases rapidly with increasing  $y/H$  ( $H$  being the height of the channel). The experimental data and the numerical simulation results of Tsuji et al. (1989) are also reproduced in this figure for comparison. Tsuji et al. (1989) used a Lagrangian trajectory analysis procedure for their particulate phase, which also allowed for collisional interactions. The present model prediction appears to be in good agreement with the simulation result of Tsuji et al. (1989). But both model predictions deviate somewhat from the experimental data. As pointed by Tsuji et al. (1989), this is mainly because the particles used in their experiment were not perfectly spherical. In fact, their experimental data showed that a small deviation of particle shapes from perfect spheres has a significant effect on the concentration profile.

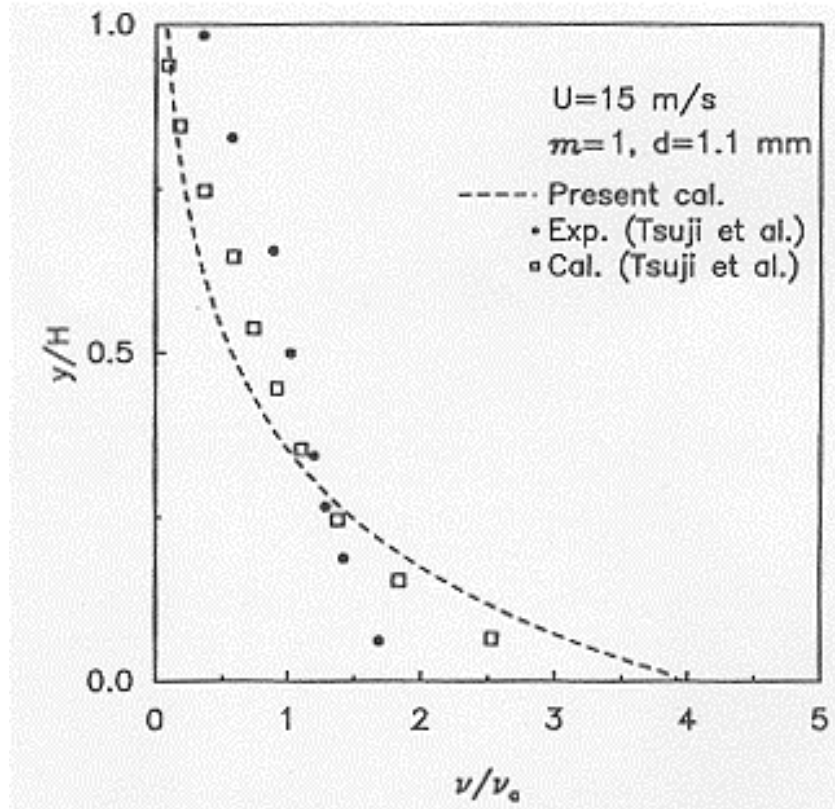


Figure 16. Variations of solid volume fraction profile in a horizontal duct. Comparison with the data and model of Tsuji et al. (1989).

#### 4. EULERIAN VOF ANALYSIS OF BUBBLE COLUMN

An Eulerian Volume of Fluid (VOF) model for analyzing the flow condition in the bubble column was developed. The FLUENT code was used to evaluate the unsteady liquid-gas flows in the bubble column. Lagrangian particle tracking approach was then used to analyze the motion of particles. Sample results of this approach are described in this section. The height of the column is 1 m with a width of 20 cm. Air enters from 1-mm holes at the bottom of the column. Figure 17 shows the concentration contours in the column at 1.16 second after the startup. (The gravity points from right to left in this figure.) The initial stages of air bubble formation are observed from this figure.

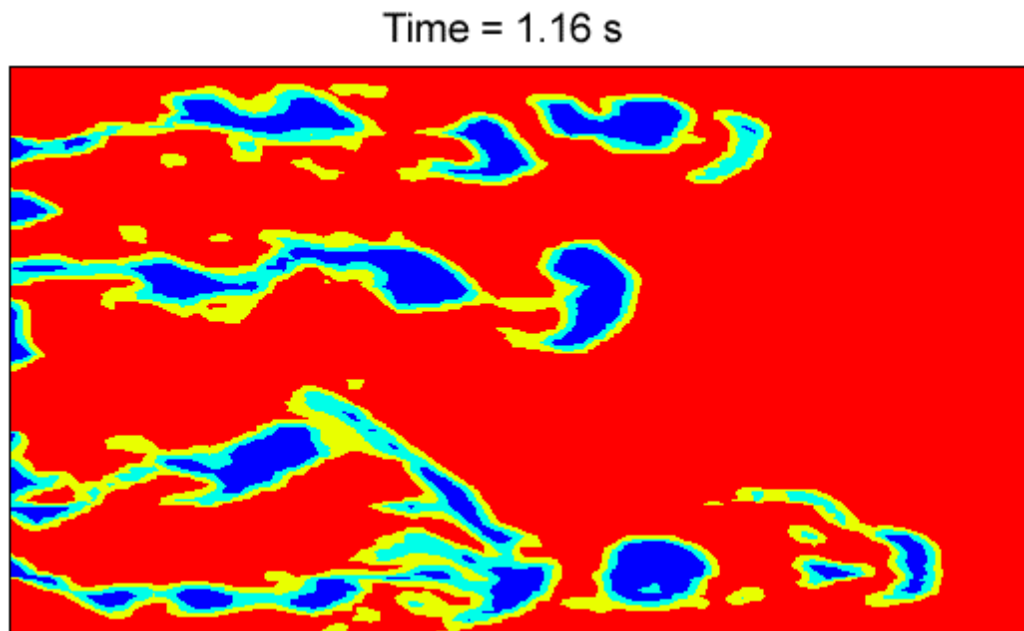


Figure 17. Concentration contours in the bubble column at  $t = 1.16$  s.

The velocity vector field in the bubble column and the concentration contours at  $t = 1.16$  s are shown in Figure 18. It is noticed that the formation of gas bubble leads to rather complex flow pattern in the column. Figure 19 shows the corresponding concentration contours and sample trajectories for  $100\ \mu\text{m}$  particles. It is observed that some particles paths ends up in the bubble, while some others pass through the gas bubbles. This depends on the relative velocity between the bubble and the particle. (Here the mean particle trajectories were analyzed using the frozen field approach.)

Time = 1.16 s

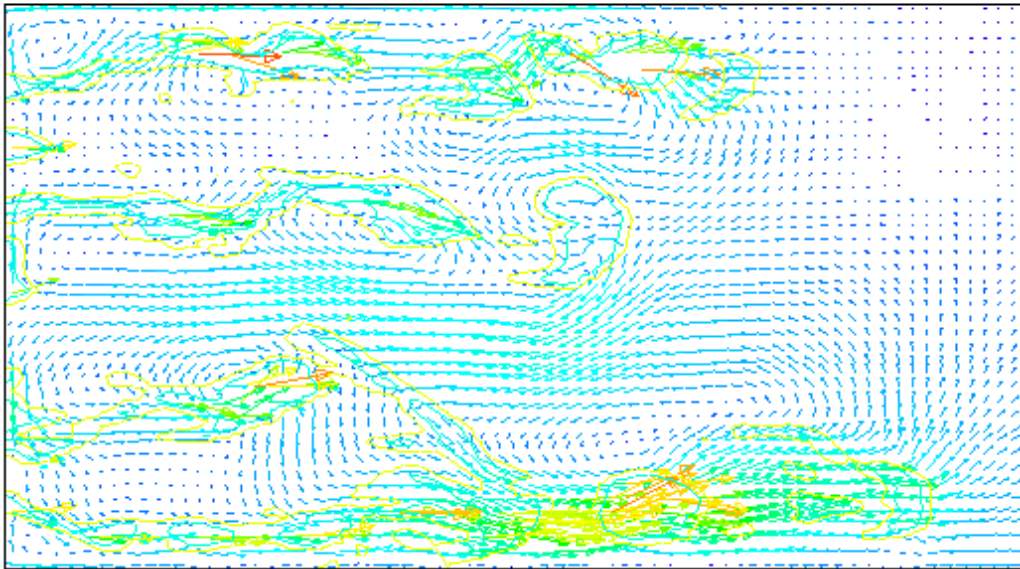


Figure 18. The velocity vector plot and concentration contours in the bubble column at  $t = 1.16$  s.

Time = 1.16 s

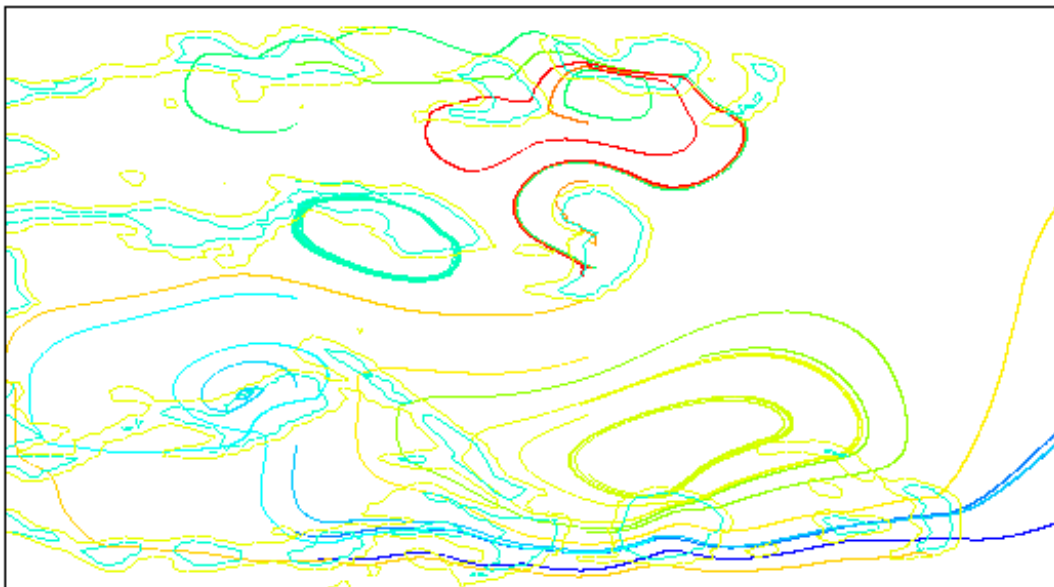


Figure 19. Concentration contours and sample particle trajectories in the bubble column at  $t = 1.16$  s.

Figure 20 shows the variation of the velocity vector field and the concentration contours at  $t = 9.3$  s. The bubble column is nearly fully developed at this time and contains many large and small gas bubbles. Formation of several recirculating flow regions in the bottom of the vessel can be clearly seen from this figure. Sample mean trajectories for  $100\ \mu\text{m}$  particle are also shown in this figure for comparison. The mean particle trajectories form loops in the recirculating flow regions. Figure 21 shows the corresponding particle trajectories when the effect of turbulence dispersion is included in the analysis. It is observed that the turbulence fluctuation field causes the particle to significantly disperse.

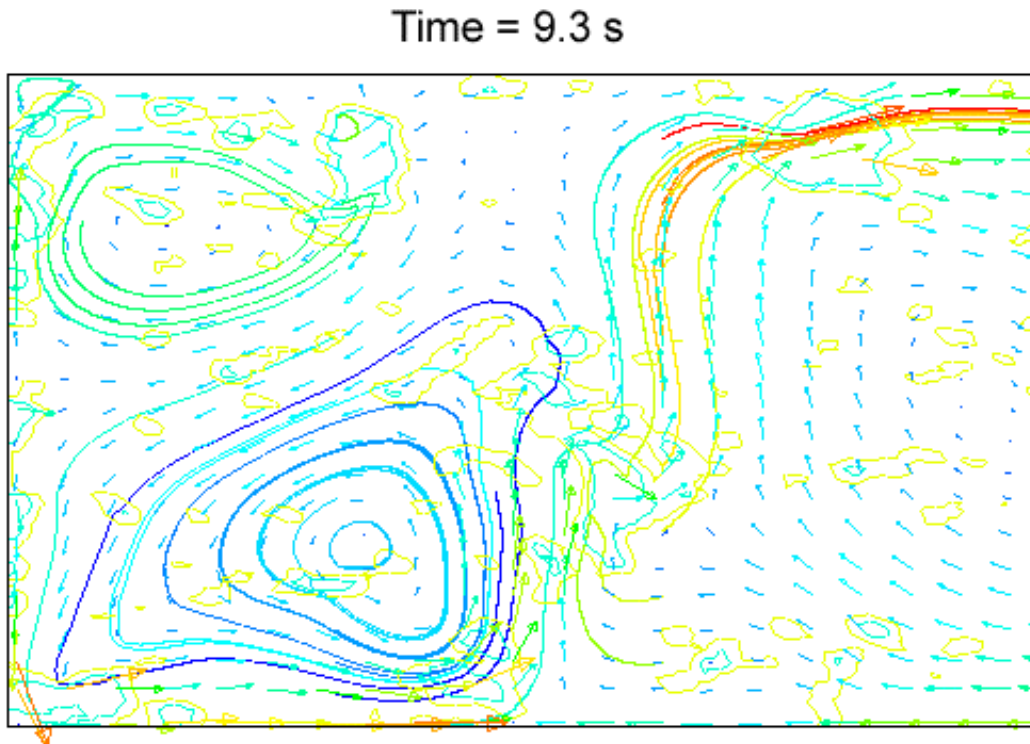


Figure 20. Concentration contours, velocity vector plot and sample mean particle trajectories in the bubble column at  $t = 9.3$  s.

Time = 9.3 s

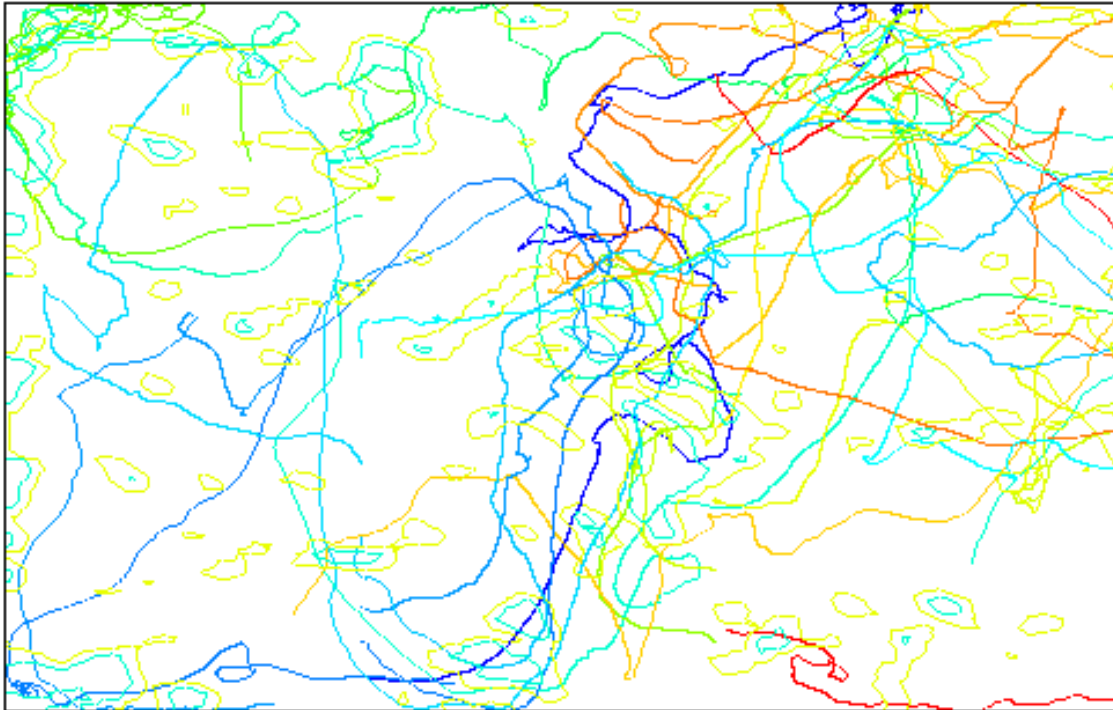


Figure 21. Concentration contours and sample random particle trajectories in the bubble column at  $t = 9.3$  s.

## ARTICLES, PRESENTATIONS AND STUDENT SUPPORT

### Journals Articles (peer reviewed)

He, C. and Ahmadi, G., Particle Deposition in a Nearly Developed Turbulent Duct Flow with Electrophoresis, *J. Aerosol Science*, Vol. 30, pp. 739-758 (1999).

Cao, J. and Ahmadi, G., Gas-Particle Two-Phase Flow in Horizontal and Inclined Ducts, *Int. J. Engng. Sci.*, Vol. 38, pp. 1961-1981 (2000).

Zhang, H. and Ahmadi, G., Aerosol Particle Transport and Deposition in Vertical and Horizontal Turbulent Channel Duct Flows, *J. Fluid Mechanics*, Vol. 406, pp. 55-88 (2000).

Fan, F-G. and Ahmadi, G., Wall Deposition of Small Ellipsoids from Turbulent Air Flows-A Brownian Dynamics Simulation, *J. Aerosol Sci.*, Vol. 31, pp. 1205-1229 (2000).

Soltani, M. and Ahmadi, G., Direct Numerical Simulation of Curly Fibers in Turbulent Channel Flow, *Aerosol Science Technology*, Vol. 33, pp. 392-418 (2000).

Ahmadi, G., He, C., Ban, H. and Stencel, J.M., Air Flow and Particle Transport in Triboelectric Coal/Ash Cleaning System-Counter Flowing Straight Duct Design, *Particulate Science Technology*, Vol. 18, pp. 213-256 (2000).

Shams, M., Ahmadi, G. and Rahimzadeh, H., A Sublayer Model for Deposition of Nano- and Micro-Particles in Turbulent Flows, *Chemical Engineering Science*, Vol. 55, pp. 6097-6107 (2000).

Zhang, H. and Ahmadi, G., Aerosol Particle Removal and Re-entrainment in Turbulent Flows- A Direct Numerical Simulation Approach, *J. Adhesion*, Vol. 74, pp. 441-493 (2000).

Zhang, H., Ahmadi, G., Fan, F.-G. and McLaughlin, J.B., Ellipsoidal Particles Transport and Deposition in Turbulent Channel Flows, *International Journal Multiphase Flows*, Vol. 27, pp. 971-1009 (2001).

Zhang, H. and Ahmadi, G., Particles Transport and Deposition in the Hot-Gas Filter Vessel at Wilsonville, *Powder Technology*, Vol. 116, pp. 53-68 (2001).

Ahmadi, G. and C. He, Simulation of Particles Transport and Deposition in a Combustor, *Chemical Engineering Communication*, Vol. 187, pp. 23-53 (2001).

Mansoori, Z., Saffar-Avval, M., Basirat Tabrizi, H and Ahmadi, G., Modeling of Heat Transfer in Turbulent Gas-Solid Flow, *International Journal Heat Mass and Transfer*, Vol. 45, pp. 1173-1184 (2002).

Mansoori, Z., Saffar-Avval, M., Basirat Tabrizi, H., Ahmadi, G., and Lain. S., Thermo-Mechanical Modeling of Turbulent Heat Transfer in Gas-Solid Flows Including Particle Collisions, *International Journal of Heat and Fluid Flow*, Vol. 23, pp. 792-806 (2002).

Ahmadi, G. and Smith, D.H., Gas Flow and Particle Deposition in the Hot-Gas Filter Vessel of the Pinon Pine Project, *Powder Technology* Vol. 128, pp. 1–10 (2002).

Gamwo, I.K., Halow, J.S. and Ahmadi, G., Nonisothermal Simulation of Flows in the Hot-Gas Filter Vessel at Wilsonville, *Particulate Science and Technology*, Vol. 20, pp. 45-58 (2002).

Mazaheri, A.R., Ahmadi, G., and Gamwo, I., Hot-Gas Flow and Particles Transport and Deposition in a Candle Filter Vessel, *Advanced Powder Technology*, Vol. 14, pp. 111-125 (2003).

Ahmadi, G., He, C., Smith, D.H. and Ramer, Everett, Gas Flow and Particle Transport and Deposition in a Pilot –Scale Furnace, *Particulate Science Technology*, Vol. 21, pp. 375-386 (2003).

Ahmadi, G., Mazahri, A.R. and, Smith, D.H. A Model for Multiphase Flows through Poroelastic Media, *Journal Porous Media*, Vol. 6, pp. 1-14 (2003).

Chrigui, M., Sadiki, A. and Ahmadi, G., Study of Interaction in Spray between Evaporating Droplets and Turbulence Using Second Order Turbulence RANS Modelling and a Lagrangian Approach, *Progress in Computational Fluid Dynamics*, Vol. 4, pp. 162-174 (2004).

## **Conference Presentations**

G. Ahmadi and J. Cao, "Anisotropic Model for Granular and Dense two-Phase Flows," 1999 ASME Mechanics and Materials Conference, Blacksburg, VA, June 27-30, 1999.

G. Ahmadi, K. Elliott and W. Kvasnak, "An Experimental Study of Granular Flow in a Couette Flow Device," 1999 ASME Mechanics and Materials Conference, Blacksburg, VA, June 27-30, 1999.

C. He and G. Ahmadi, "Modeling of Particle Dispersion and Deposition with Thermophoresis in a Controlled Profile Combustor," 18th Annual Conference of the American Association for Aerosol Research, AAAR '99, Tacoma, WA, October 11-15, 1999.

H. Zhang and G. Ahmadi, "Aerosol Particle Removal and Re-entrainment in Turbulent Channel Flows," 18th Annual Conference of the American Association for Aerosol Research, AAAR '99, Tacoma, WA, October 11-15, 1999.

H. Zhang and G. Ahmadi, F. Fan and J.B. McLaughlin, "Analysis of the Motion of Ellipsoidal Particle in Turbulent Channel Flows," 52st Annual Meeting of American Physical Society, Division of Fluid Dynamics, New Orleans, LA, November 21-23, 1999.

P.V. Skudarnov, L.L. Regel, W. R. Wilcox and G. Ahmadi, "Numerical Modeling and Flow Visualization in the Gradient Freeze Configuration During Centrifugation," Fourth International Workshop on Materials Processing at High Gravity, Clarkson University, Potsdam, NY, May 29-June 2, 2000.

A.R. Mazaheri, H. Zhang and G. Ahmadi, "A Centrifugal Filtration Concept for Hot-Gas Cleaning," Fourth International Workshop on Materials Processing at High Gravity, Clarkson University, Potsdam, NY, May 29-June 2, 2000.

G. Ahmadi, "Advanced Computational Model for Three-Phase Slurry Reactors," Abstract and Research Accomplishments of University Coal Research Projects, pp. 91-91, University Coal Research Contractors Review Conference, NETL, Pittsburgh, PA, June 6-7, 2000.

G. Ahmadi and H. Zhang, "Resuspension of Particles in Turbulent Flows," Seventh International Symposium on Particles on Surfaces: Detection, Adhesion and Removal, Newark, NJ, June 19-21, 2000.

G. Ahmadi and H. Zhang, "Hot-Gas Flow and Particle Transport and Deposition in the Filter Vessel at Wilsonville," Seventeenth Annual International Pittsburgh Coal Conference, Pittsburgh, PA, September 11-14, 2000.

A.R. Mazaheri and G. Ahmadi, "Computational Modeling of a Centrifugal Filtration System," 19th Annual Conference of the American Association for Aerosol Research, AAAR 2000, St. Louis, MO, November 6-10, 2000.

D.J. Schmidt, G. Ahmadi, and G. Schmidt, "Dispersion of Droplets in a Turbulent Spray," 19th Annual Conference of the American Association for Aerosol Research, AAAR 2000, St. Louis, MO, November 6-10, 2000.

M. Shams, G. Ahmadi and H. Rahimzadeh, "Transport and Deposition of Flexible Fibers in Turbulent Flows," 19th Annual Conference of the American Association for Aerosol Research, AAAR 2000, St. Louis, MO, November 6-10, 2000.

H. Zhang, G. Ahmadi, R. Han and B.J. Greenspan, "Impact Breakup of Particle Pairs," 19th Annual Conference of the American Association for Aerosol Research, AAAR 2000, St. Louis, MO, November 6-10, 2000.

H. Zhang, G. Ahmadi, R. Han and B.J. Greenspan, "Breakup of Pairs of Attached Particles in Simple Shear Flows," 19th Annual Conference of the American Association for Aerosol Research, AAAR 2000, St. Louis, MO, November 6-10, 2000.

D.J. Schmidt, G. Ahmadi, and G. Schmidt, "Lagrangian PDF: Application to Multiphase Spray Simulation," 4th International Conference on Multiphase Flows, ICMF' 2001, New Orleans, LA, May 27-June 1, 2001.

C. Liu and G. Ahmadi, "Transport and Deposition of Atmospheric Particles Near a Building Model," 4th International Conference on Multiphase Flows, ICMF' 2001, New Orleans, LA, May 27-June 1, 2001.

M. Shams, G. Ahmadi and H. Rahimzadeh, "Flexible Fiber Motion in Turbulent Flows," 4th International Conference on Multiphase Flows, ICMF' 2001, New Orleans, LA, May 27-June 1, 2001.

A. Sadiki and G. Ahmadi, "A Thermodynamical Formulation for Chemically Active Multiphase Flows," Trends in Numerical and Physical Modeling for Industrial Multiphase Flows, Institut d'Etudes Scientifiques de Cargese (Corse), France, September 26-28, 2001.

A.R. Mazaheri and G. Ahmadi, "Computational Modeling of Gas Flow in an Industrial Filter Vessel," 20th Annual Conference of the American Association for Aerosol Research, AAAR 2001, Portland, Oregon, October 15-19, 2001.

A.R. Mazaheri and G. Ahmadi, "Particle Transport, Deposition and Removal with Bounce in Turbulent Channel Flow," 20th Annual Conference of the American Association for Aerosol Research, AAAR 2001, Portland, Oregon, October 15-19, 2001.

X. Zhang and G. Ahmadi, "Gas-Particle Two-Phase Flow in a Horizontal Channel," 20th Annual Conference of the American Association for Aerosol Research, AAAR 2001, Portland, Oregon, October 15-19, 2001.

C. He, and G. Ahmadi, "Particle Dispersion and Deposition in a Sudden Expansion Turbulent Pipe Flow with Electrophoresis," 20th Annual Conference of the American Association for Aerosol Research, AAAR 2001, Portland, Oregon, October 15-19, 2001.

G. Ahmadi, "Nano and Micro-Particle and Bubble Transport in Fluid Media," Annual Technical Meeting of the Center for Advanced Material Processing (CAMP), Saratoga Spring, NY, May 13-15, 2002.

A.R. Mazaheri, G. Ahmadi and H. Zhang, "Effects of Bounce on Particle Transport, Deposition and Removal in Turbulent Channel Flow," FEDSM2002-31027, Proceedings of ASME FEDSM'02, ASME Fluids Engineering Division Summer Meeting, Montreal, Quebec, Canada, July 14-18, 2002.

E. Noto, G. Ahmadi and T. Theis, "Evaluation of Bauxite Residue for Acid Mine Neutralization," AEESP/AEE Education and Research Conference, Toronto, Ontario, Canada, August 10-14, 2002.  
G. Ahmadi, A.R. Mazaheri, C. Liu, and I.K. Gamwo, "Computer Modeling of Flow, Thermal Condition and Ash Deposition in a Hot-Gas Filtration Device," 5<sup>th</sup> International Symposium on Gas Leaning at high Temperature, NETL, Morgantown, WV, September 17-20, 2002.

A.R. Mazaheri and G. Ahmadi, "Chaotic Behavior of Liquid Droplet Breakup," 21st Annual Conference of the American Association for Aerosol Research, AAAR 2002, Charlotte, NC, October 7-11, 2002.

X. Zhang and G. Ahmadi, "Turbulent Gas-Liquid-Particle Three-Phase Flows in Bubble Columns," 21st Annual Conference of the American Association for Aerosol Research, AAAR 2002, Charlotte, NC, October 7-11, 2002.

P. Zamankhan, G. Ahmadi and G. Campbell, "Numerical Simulation of Single Screw Pump-Extruder," 21st Annual Conference of the American Association for Aerosol Research, AAAR 2002, Charlotte, NC, October 7-11, 2002.

A.R. Mazaheri and G. Ahmadi, "Particle Deposition in a demonstration-Scale Filter Vessel with Ash Bridging," 21st Annual Conference of the American Association for Aerosol Research, AAAR 2002, Charlotte, NC, October 7-11, 2002.

E. M. Noto and G. Ahmadi, "A Preliminary Study of Rheological Behavior of Bauxite Residue," 21st Annual Conference of the American Association for Aerosol Research, AAAR 2002, Charlotte, NC, October 7-11, 2002.

G. Ahmadi, A. R. Mazaheri and D.H. Smith, "Multiphase Flow Through Poro-Elastic Media-A Continuum Model," IMECE2002-32492, Proceedings of ASME International Mechanical Engineering Congress, New Orleans, LA, November 17-22, 2002.

G. Ahmadi, "Modeling Aerosol Transport In Environment - Promises and Challenges," Panel on Measurement and Modeling of Environmental Flows, ASME International Mechanical Engineering Congress, New Orleans, LA, November 17-22, 2002.

X. Zhang and G. Ahmadi, "Turbulent Three-Phase Flows in Bubble Columns," American Association for Aerosol Research Particulate Matter: Atmospheric Sciences, Exposure and the Fourth Colloquium on PM and Human Health (AAAR PM) Meeting, Pittsburgh, PA, March 31 - April 4, 2003.

G. Ahmadi and X. Zhang, "Gas-Liquid-Particle Three-Phase Flows in a Bubble Column," Annual Technical Meeting of the Center for Advanced Material Processing (CAMP), Saratoga Spring, NY, May 14-16, 2003.

G. Ahmadi and A.R. Mazaheri, "Particle Removal from Plane Surfaces In Turbulent Flows," ASME Fluid Engineering Summer Conference, Honolulu, Hawaii, July 7-11, 2003.

G. Ahmadi and X. Zhang, "Gas-Liquid-Particle Three-Phase Flows in Bubble Columns," ASME Fluid Engineering Summer Conference, Honolulu, Hawaii, July 7-11, 2003.

E. Noto, G. Ahmadi, and G. Campbell, "Rheological Behavior of Bauxite Residue and Bauxite Residue Derivative," 4th International Conference on Mechanics of Time Dependent Materials, Lake Placid, NY, October 7-10, 2003.

E. Noto, G. Ahmadi, and G. Campbell, "Characterization of Bauxite Residue and Derivatives at Varying pH Values," 75th Annual Meeting of Society of Rheology, Pittsburgh, PA, October 12-16, 2003,

X. Zhang and G. Ahmadi, "Numerical Simulation of Three-Phase Bubbly Flows in a Bubble Column," Fall Technical Meeting of the Center for Advanced Material Processing (CAMP), Potsdam, NY, October 16, 2003.

A.R. Mazaheri, G. Ahmadi, and D.H. Smith, "Multiphase Flows through Porous Media," 22nd Annual Conference of the American Association for Aerosol Research, AAAR 2003, Anaheim, CA, October 20-24, 2003.

W. Chen, G. Ahmadi and J. Taylor, "On Bubble Motions in Simple Shear Flows," 22nd Annual Conference of the American Association for Aerosol Research, AAAR 2003, Anaheim, CA, October 20-24, 2003.

X. Zhang and G. Ahmadi, "Three-Phase Turbulent Flows in a Bubble Column," 22nd Annual Conference of the American Association for Aerosol Research, AAAR 2003, Anaheim, CA, October 20-24, 2003.

G. Ahmadi, "Computational Modeling of Multiphase Flows – Environmental Applications," (Invited

Lecture) Third International Symposium on Advanced Fluid Information, AFI-2003, New York, NY, November 21-22, 2003. Also in AFI-2003, Fluid-Informatics for Biomedical and Environmental Quality Applications, Ed. H. Higuchi and T. Hayase, pp. 15-20, 2003.

W. Chen and G. Ahmadi, "Distribution of Gas Holdup in a Bubble Column," Annual Technical Meeting of the Center for Advanced Material Processing (CAMP), Canandaigua, NY, May 12-14, 2004.

X. Zhang and G. Ahmadi, "Numerical Simulation of Turbulent Three-Phase Bubbly Flows in a Bubble Column," Annual Technical Meeting of the Center for Advanced Material Processing (CAMP), Canandaigua, NY, May 12-14, 2004.

K. Nazridoust and G. Ahmadi, "Multiphase Fluid Flow Through an Artificially Induced CT-Scanned Fracture," Annual Technical Meeting of the Center for Advanced Material Processing (CAMP), Canandaigua, NY, May 12-14, 2004.

G. Ahmadi, "Fiber Transport and Deposition in Turbulent Flows," ASME Heat Transfer/Fluid Engineering Summer Conference, Charlotte, NC, July 11-15, 2004.

G. Ahmadi, A.R. Mazaheri and D.H. Smith, "Multiphase Flows Through Fractured Rocks," ASME Heat Transfer/Fluid Engineering Summer Conference, Charlotte, NC, July 11-15, 2004.

G. Ahmadi, Z. Mansoori, M. Saffar-Avval, and H. Bassirat Tabrizi, "Gas-Solid Turbulent Flows with Heat Transfer Including Particle Collisions," ASME Heat Transfer/Fluid Engineering Summer Conference, Charlotte, NC, July 11-15, 2004.

A.R. Mazaheri, G. Ahmadi, D.H. Smith, B. Zerai, M. Oliver, J.R. Kadambi, and B.Z. Saylor, "A Study of Flow Through Lattice Cell Model," ASME Heat Transfer/Fluid Engineering Summer Conference, Charlotte, NC, July 11-15, 2004.

## **Students and Collaborators**

- X. Zhang, graduate (Ph.D.) student, Mech. & Aero. Engineering, Clarkson University.
- W. Chen, graduate (Ph.D.) student, Mech. & Aero. Engineering, Clarkson University.
- A.R. Mazaheri, graduate (Ph.D.) student, Mech. & Aero. Engineering, Clarkson University  
(Currently NRC Fellow at NETL, DOE)
- J. Cao, graduate (Ph.D.) student, Mech. & Aero. Engineering, Clarkson University.  
(Currently with NMNA)
- H. Zhang, graduate (Ph.D.) student, Mech. & Aero. Engineering, Clarkson University  
(Currently with ASYST Technology)

- C. He, graduate (Ph.D.) student, Mech. & Aero. Engineering, Clarkson University (Currently with Corning)
- W. Kvasnak, graduate (Ph.D.) student, Mech. & Aero. Engineering, Clarkson University (Currently with Pratt & Whitney)